UNIVERSITY OF LEEDS

This is a repository copy of *Reaction Kinetics of Meteoric Sodium Reservoirs in the Upper Atmopshere*.

White Rose Research Online URL for this paper:
http://eprints.whiterose.ac.uk/86103/

White Rose
university consortium
Universities of Leeds, Sheffield & York

eprints@whiterose.ac.uk
https://eprints.whiterose.ac.uk/

Reaction Kinetics of Meteoric Sodium Reservoirs in the Upper Atmosphere

J. C. Gómez Martín, S. A. Garraway and J. M. C Plane[*]

School of Chemistry, University of Leeds, Woodhouse Lane, LS2 9JT, Leeds, UK

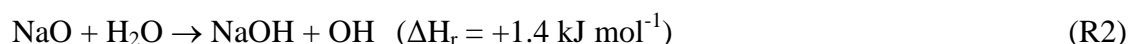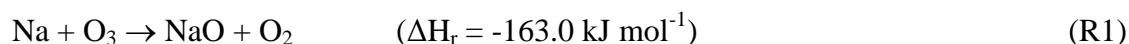[*]Correspondence to: J.M.C.Plane@leeds.ac.uk

Abstract

The gas-phase reactions of a selection of sodium-containing species with atmospheric constituents, relevant to the chemistry of meteor-ablated Na in the upper atmosphere, were studied in a fast flow tube using multi-photon ionisation time-of-flight mass spectrometry. For the first time unambiguous observations of NaO and NaOH in the gas phase under atmospheric conditions have been achieved. This enabled the direct measurement of the rate constants for the reactions of NaO with H_2, H_2O and CO, and of NaOH with CO_2, which at 300-310 K were found to be (at 2σ confidence level): $k(NaO + H_2O) = (2.4 \pm 0.6) \times 10^{-10}$ cm^3 molecule^{-1} s^{-1}, $k(NaO + H_2) = (4.9 \pm 1.2) \times 10^{-12}$ cm^3 molecule^{-1} s^{-1}, $k(NaO + CO) = (9 \pm 4) \times 10^{-11}$ cm^3 molecule^{-1} s^{-1}, and $k(NaOH + CO_2 + M) = (7.6 \pm 1.6) \times 10^{-29}$ cm^6 molecule^{-2} s^{-1} (P = 1 - 4 Torr). The NaO + H_2 reaction was found to make NaOH with a branching ratio $\geq$ 99%. A combination of quantum chemistry and statistical rate theory calculations are used to interpret the reaction kinetics and extrapolate the atmospherically relevant experimental results to mesospheric temperatures and pressures. The NaO + H_2O and NaOH + CO_2 reactions act sequentially to provide the major atmospheric sink of meteoric Na, and therefore have a significant impact on the underside of the Na layer in the terrestrial mesosphere: the newly determined rate constants shift the modelled peak to about 93 km, i.e. two km higher than observed by ground-based lidars. This highlights further uncertainties in the Na chemistry cycle such as the unknown rate constant of the NaOH + H reaction. The fast Na-recycling reaction between NaO and CO and a re-evaluated rate constant of the NaO + CO_2 sink should be now considered in chemical models of the Martian Na layer.
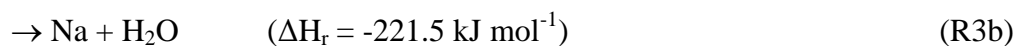
Keywords: Mesosphere, Meteoric Metal Layers, Sodium Chemistry, Photo-ionisation Mass Spectrometry.

1. Introduction

The atmospheres of the Earth and of other solar system bodies receive a large input of interplanetary dust particles (IDPs). IDPs enter at hyperthermal speeds and heat rapidly due to collisions with air molecules, which can cause the particles to melt and the metallic constituents to ablate. In the Earth's atmosphere, for which the IDP mass input rate remains highly uncertain (5-300 t d^{-1} [1]), meteoric ablation occurs between 70 and 120 km in the mesosphere/lower thermosphere (MLT) region, giving rise to the neutral and ionic layers of metallic elements including Na, K, Fe, Mg and Ca. These metals are believed to play a role in a number of important atmospheric phenomena, such as the nucleation of noctilucent clouds and stratospheric aerosols.[2]

Historically the study of the Na layer facilitated the understanding not only of the gas-phase chemistry of sodium but also of the chemistry and dynamics of the mesosphere as a whole.[3] Explaining the presence of the Na layer in the upper mesosphere and its variability has required investigating the major Na reservoirs and sinks, especially regarding their photolysis and photo-ionisation cross sections, and temperature-dependent rate constants. Above the Na layer, which peaks around 90 km, ion chemistry dominates: Na$^+$ ions are formed by charge transfer of Na with NO$^+$ and O$_2^+$ and by photo-ionisation. The formation of ion clusters, followed by dissociative electron recombination, leads to neutralization of Na$^+$. Below 90 km Na is converted into less reactive neutral species:

$$Na + O_3 \rightarrow NaO + O_2 \qquad (\Delta H_r = -163.0 \text{ kJ mol}^{-1}) \qquad (R1)$$

$$NaO + H_2O \rightarrow NaOH + OH \quad (\Delta H_r = +1.4 \text{ kJ mol}^{-1}) \qquad (R2)$$

$$NaO + H_2 \rightarrow NaOH + H \qquad (\Delta H_r = -60.0 \text{ kJ mol}^{-1}) \qquad (R3a)$$

$\rightarrow Na + H_2O$ $\qquad$ (ΔH_r = -221.5 kJ mol^{-1}) $\qquad$ (R3b)

$NaOH + CO_2 + M \rightarrow NaHCO_3 + M$ $\qquad$ (ΔH_r = -132.0 kJ mol^{-1}) $\qquad$ (R4)

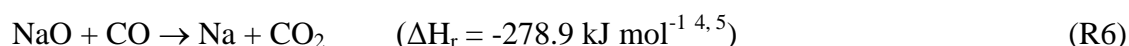The reaction enthalpies at 298 K for R1-3 have been calculated using evaluated enthalpies of formation [4-6] and considering the $NaO(X^2\Pi)$ ground state. For R4, we have calculated the reaction enthalpy at 298 K at the CBS-QB3 level of theory,[7] using the Gaussian09 suite of programs.[8]

The key reactions 2 and 3 form the reservoir NaOH. Apart from photolysis, there is only one known path (NaOH + H $\rightarrow$ Na + H$_2$O [9, 10]) back to the reactive species Na, NaO and NaO$_2$, which interconvert rapidly via photolysis and reactions with O, O$_2$ and O$_3$.[2] Previous studies on R2 and R3 [11, 12] indicate that R2 is the most important source of NaOH in the terrestrial atmosphere, whereas R3 would predominate in hydrogen-rich planetary atmospheres. NaHCO$_3$ acts as a reservoir species for Na because it is a stable, closed-shell molecule. The only routes which reform Na from NaHCO$_3$ are photolysis [13] and reaction with atomic H [14] (both slow). In Mars, the low mixing ratios of H$_2$ and H$_2$O make R5 the major sink for meteoric Na:

$NaO + CO_2 + M \rightarrow NaCO_3 + M$ $\qquad$ (ΔH_r = -177.3 kJ mol^{-1}, CBS-QB3, 298 K) (R5)

whereas the reaction:

$NaO + CO \rightarrow Na + CO_2$ $\qquad$ (ΔH_r = -278.9 kJ mol^{-1} [4, 5]) $\qquad$ (R6)
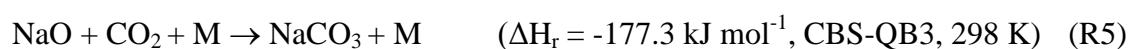
may play a similar role to the NaO + O reaction in the Earth's mesosphere.[15]

Studies on R2-6 are scarce in the literature. R2 was investigated previously by Ager and Howard [11] and by Cox and Plane,[12] with the reported rate constants differing by a factor of

~3. In order to monitor the NaO concentration, Ager and Howard titrated NaO with NO to produce Na atoms, which could then be detected via resonance fluorescence at 590 nm. Cox and Plane's detection of NaO was based on its chemiluminescent reaction with atomic oxygen. Reaction R2 has attracted some fundamental interest in the past due to the substantial long-range attractive force between the large dipole moments of the reagent molecules on the one hand, and its close to zero reaction enthalpy change on the other.[12, 16] R3 was investigated previously only by Ager and Howard,[11] who observed both channels, although the branching ratio $\alpha = k_{3b}/k_3$ was not quantified. The pressure-dependent rate constants of R4 and R5 were measured by Ager and Howard [17, 18] who titrated NaOH and NaO with H and NO, respectively, to make Na. The rate constant of R6 has not been reported previously.

A common feature to all these previous studies is the use of indirect techniques for monitoring the concentrations of NaO and NaOH, generally involving chemical conversion to Na. The low vapor pressures and potentially rapid polymerisation of these compounds cause heavy losses in reactors and flow tubes, and therefore extremely sensitive detection techniques are required. To the best of our knowledge, laser induced fluorescence (LIF) of NaO in the UV-vis spectral region has never been observed. NaO LIF in the 668-725 nm region was suggested to correspond to the B-X electronic transition of NaO and proposed as a possible means to detect NaO,[19] but this scheme does not appear to be useful in measuring NaO reaction kinetics. Indeed, our group has unsuccessfully attempted in the past LIF detection of NaO in this spectral region, which led us to suspect that the LIF spectra reported by Pugh et al.[19] does not correspond to a ground state transition. An important drawback of spectroscopic and chemical conversion techniques is that these target a single species at a time. Multiplexed observation of sodium oxides and hydroxides using mass spectrometry has been reported previously at high temperatures, in vaporisation, pick-up and crossed molecular beam arrangements, mainly in the context of thermochemical analysis and molecular

electronic structure studies,[20-28] but the observation of sodium compound kinetics at thermal energies has remained elusive for mass spectrometric techniques.

In this paper we present a new experimental set-up combining photo-ionisation (PI) with time-of-flight mass spectrometry (ToF-MS), which for the first time enables direct observation of NaO and NaOH at relatively low temperatures, and therefore allows direct measurement of rate constants of their reactions with atmospheric constituents. Additionally, the rate constants of the reactions of N_2O with Na and Na_2 have been measured in order to validate the set-up using a well-studied reaction and to investigate the origin of the prominent m/z 62 (Na_2O^+) peak, respectively. The results are interpreted using a combination of ab initio quantum calculations and master equation modelling of the observed rate constants. Finally, implications for the sodium atmospheric chemistry of the Earth and Mars are discussed.

2. Experimental

2.1. Fast Flow Tube

Fig. 1 is a schematic diagram of the fast flow tube coupled to the new PI-ToF-MS system developed to investigate the chemistry of meteoric metal reservoir molecules and clusters. The flow tube is made up of cross-pieces and nipple stainless steel sections connected by conflat flanges and sealed with copper gaskets. It has an internal diameter of 38 mm and an adjustable length between 30 and 60 cm. A flow of inert gas (N_2), typically 2.5 standard litres per minute (slm), is used to carry the reactants down the tube towards the sampling point. The Na source (oven) is placed in a perpendicular side arm and consists of a 16 mm internal diameter conflat nipple fitted internally with a metallic mesh tube packed with atomic sodium

pellets, which can be heated up to 700 K using a bundle of cartridge heaters wrapped around the outer wall.[3] A temperature controller ensures that the temperature inside the oven remains stable within 0.5 K. A flow of N_2 (typically 500 standard cubic centimetres per minute, sccm) is passed though the oven and carries the sodium vapor to the core of the main carrier gas flow by means of a copper tube section which protrudes perpendicularly from the oven into the flow tube. Downstream of the oven source, the flow tube is fitted with a 4-way cross through which atomic resonance absorption measurements of the atomic Na concentration in the tube can be performed. The light from a Na hollow cathode lamp is directed perpendicular to the flow tube axis and then focused into the entrance slit of a small monochromator (Optometrics, Mini-Chrom MC1-02) coupled to a photomultiplier (Hamamatsu H7710-12). The monochromator is set to the wavelength of the sodium D2 line (589.0 nm). The extent of light absorption by atomic sodium can be linked to its average concentration across the flow tube diameter via the Beer-Lambert law,[29] by knowing the optical path length and the average absorption cross section of the 589.0 nm sodium D line ($\sim 1 \times 10^{-11}$ cm^2 [30]). Typical Na concentrations in the source region were around 10^{12} atom cm^{-3}.

The pressure and temperature at the oven and in the flow tube are measured using calibrated capacitance manometers (Baratron) and T-type thermocouples (Omega), respectively. The accessible range of pressure is 0.5-8 Torr, determined by the maximum operational pressure inside the high vacuum ToF-MS chamber. In the experiments reported here the average temperature within the reaction zone was typically between 300 K and 310 K. Under these conditions, the Reynolds number was maintained in the 50-200 range, i.e. within the laminar flow regime. Flow characterisation experiments were carried out with a pulsed source (laser ablation of atomic Fe from a rotating iron rod [31]) showing that the arrival time of a Fe atom pulse from the metal source (Fig. S1a) is consistent with a fully developed parabolic velocity

6

profile. Under low pressure, diffusion-controlled conditions, the linear velocity at the core of the laminar flow v_p is a factor 1.6 larger than the average linear velocity v /cm s^{-1} of the carrier flow [32, 33], calculated from pressure (P /Torr), temperature (T /K), flow rate (F /sccm), and tube radius (r /cm):

$$v = 1.477 \times 10^{-8} \frac{F\,T}{P\,r^2} \qquad\qquad (E1)$$

Indeed, in our system a regression of the calculated vs. observed pulsed ablation Fe peak arrival times yields a slope of 1.59, with a 2σ uncertainty of ~8% (Fig. S1b).

In order to sustain detectable concentrations of sodium species at the detection point, the oven had to be heated to temperatures generally higher than 600K, which caused a significant axial temperature gradient inside the flow tube. This gradient was characterised by using a movable thermocouple which could be placed at different points between the Na source and the sampling point. In this way the downstream section of the tube within which the temperature gradient was tolerable (± 5 K) was determined (this section extended from 150-200 mm downstream of the oven to the MS sampling pinhole). Similarly, a radial parabolic temperature profile was observed using a sliding thermocouple inserted from a wall port, consistent with the development of a laminar flow. The slow heat transfer which causes the radial gradient mirrors the slow transfer of matter by diffusion though the laminae from the core of the flow to the walls of the tube, which is key in order to enable detection of species such as NaO and NaOH after a ~20 ms flight time. Some lower temperature experiments were also carried out by packing chips of solid CO_2 around the flow tube. However, due to the high temperature of the oven and the aforementioned slow heat transfer and, the temperature at the core of the flow could only be reduced to 266 K.

NaO was produced in situ by fast conversion of the flow of Na atoms at the oven outlet by addition of a large excess of N_2O to the main carrier flow:

$$Na + N_2O \rightarrow NaO + N_2 \qquad (\Delta H_f = -102.4 \text{ kJ mol}^{-1}) \qquad \qquad (R7)$$
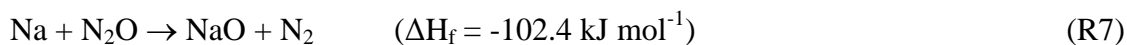
The NaO was then carried further down the flow tube to where reaction occurred with an excess of reactant gas added through the sliding injector. Similarly, NaOH could be generated in the upstream section of the flow tube by adding H_2O or H_2 (R2 and R3) to the main carrier flow containing also a fraction of N_2O.

Experiments were performed under pseudo-first order conditions, i.e. the reagent was in large excess over the sodium-containing species of interest. The reactant flow (R = H_2, H_2O, CO, CO_2) was set with a calibrated mass flow controller (MKS) and entrained into the main flow by using an off-axis glass sliding injector, with the aperture facing upwards towards the core of the flow. For a given injection point, experiments were carried out by changing the concentration of reactant gas, [R], while the total flow of gas was kept constant by means of a balance N_2 flow. In addition, sets of experiments were conducted with the tip of the injector at different distances from the source, in order to change the effective contact time t_{eff} between NaX (X = O, OH) and reactant.

2.2. PI-ToF-MS

The gas in the flow tube is sampled on-axis from the core of the laminar flow via an earthed skimmer cone with a 200 μm pinhole using a scroll pump-backed turbo-molecular pump. PI of the relevant Na-containing molecules takes place in the ionisation chamber (P = 10^{-4}-10^{-5} Torr) before mass spectrometric detection. This chamber is fitted with viewports which allow a 10 Hz pulsed laser beam to be directed through the high density region of the sampled gas

jet. Alternatively, a built-in electron gun can be used to carry out 15-100 eV electron impact ionisation.

A range of soft PI schemes is available for these experiments. The basic set-up employs a frequency-tripled Nd:YAG laser (Continuum Surelite 10-II) at 355 nm. The laser beam can be used directly or by pumping a dye laser (Sirah Cobra Stretch). Single photon vacuum ultraviolet (VUV) ionisation can be implemented via frequency tripling by tight focusing of the 355 nm or the dye laser beam in a rare gas cell. [34] This technique has previously been shown to be suitable for the detection of organic molecules. [35] Using the 355 nm beam to produce 118 nm radiation (10.5 eV) gives, for example, an excellent detection limit for acetone in our system (10^{11} molecule cm^{-3} in a single accumulation in analogue mode). The conversion efficiency of frequency tripling in a rare gas is rather low (~10^{-5}),[36] and therefore this approach is only useful with molecules with substantial PI cross sections (>10^{-18} cm^2 molecule^{-1}). Possible interference from the fundamental, if not separated from the VUV third harmonic, needs to be considered as well.[37] This is particularly relevant for molecules with UV-vis absorption bands such as the alkali metal-containing oxides and hydroxides. For example, NaO and NaOH show large absorption bands around 315 nm which can lead to photolysis or (single colour) two-photon ionisation.[13] Indeed, this suggests an alternative to single photon VUV ionisation, since multi-photon ionisation can be particularly efficient if resonances with excited states of the target species exist. For NaO and NaOH, we show below that tuning the dye laser wavelength to the peak of their UV absorption bands and focussing the laser beam in the ionisation chamber enables detection of these two species. Dye solutions were prepared to generate photons in 3 different spectral ranges after frequency doubling using a BBO or KDP crystal: pyridine 2 (365 nm - 350 nm), DCM (305 nm - 325 nm) and Coumarin 440 (215 nm - 225 nm). Typical laser powers were ~25 mJ pulse^{-1} for the 355 nm beam and ~8 mJ pulse^{-1} for the 315 nm beam.

The positive (negative) ions resulting from PI of molecules in the sampled gas jet are accelerated towards the custom-made ToF-MS (Kore) by means of a pulsed negative (positive) voltage. After extraction, the ions are focused though a differential pumping aperture by a high voltage lens element, before being formed into a roughly parallel beam that enters the ToF-MS at the field free region potential (P = 10^{-7}-10^{-9} Torr). Two pairs of biased plates are used to bend the ion beam in order to direct it towards the detector side of the flight tube. Before hitting the detector, the ions fly in the field free region on the way to and back from a reflectron with a typical potential of -1.6 kV, which for any given ion m/z reduces the flight-time dependence on drift energy, thus improving resolution. The resolution at m/z 23 (Na^+) is 0.07 amu FWHM, which increases up to ~0.5 amu FWHM at m/z 209 ($Na_7O_3^+$). A Bradbury-Nielsen (BN) gate is mounted on the entrance of the reflectron, , which allows a selected narrow m/z range to be deflected away from the detector. This is useful to filter out of the mass spectrum any intense peak which would otherwise saturate the detector.

The dual michrochannel plate detector has a floatable polarity and can be used alternatively for positive and negative ions. A pre-amplifier coupled to the detector provides simultaneous analogue and digital (counting) outputs. The analogue output is useful for diagnostics and for the recording of very intense signals, which can be modulated linearly over a wide dynamic range by varying the multiplier gain. This output is registered by a digital oscilloscope (LeCroy LT342), from which mass peaks, which appear delayed in the time axis with respect to the PI laser pulse according to a characteristic time-of-flight, can be gate-integrated and passed onto a PC for accumulation and further analysis. In addition, a fast comparator is used to provide digital output pulses to a counting system (time-to-digital convertor, TDC). The Kore TDC registers ion counts within a sequence of flight-time bins referred to the initial firing of the photo-ionisation laser. This results in a histogram of counts vs time-of-flight, i.e.

a mass spectrum. A limitation of counting systems is that the signal remains proportional to concentration only for low counting rates, and so pulse counting is only useful for weak signals (low concentrations and/or low PI cross sections). The combination of simultaneous analogue and digital output results is therefore advantageous in applications where the dynamic range of m/z peak intensities is wide, as in the experiments reported here.

The PI laser and ToF-MS are synchronised using a delay generator (Quantum Composers, 9518). In every measuring cycle, the delay generator triggers the flash lamps and then the Q-switch of a Nd:YAG laser and after a few microseconds triggers the pulse extract power supply unit (and, if activated, the BN gate), which then sends a pulse to the TDC to establish the time zero event of each measuring cycle. Additionally, a pulsed metal source such as Fe laser ablation can be triggered from the delay generator. In this case the delay between the ablation and the PI laser can be scanned in order to sample the profile of the metal plume travelling down the flow tube and through the pin hole.

2.3. Data acquisition and pre-processing

In a typical experiment, 1000 digital spectra were accumulated for every reactant concentration, which at a 10 Hz laser repetition rate took 100 seconds. Once the accumulation was complete, the concentration of reactant was changed and a new accumulation started. Every few measurements a reference measurement without reactant (but with the total flow balanced) was carried out. The reference readings were used to account for instabilities in the signal, which were caused by depletion of Na in the oven, and more importantly by the blocking of the sampling pinhole due to the deposition of reaction products.

During the experiments, the integrated signal of a particular m/z peak, denoted as $S_{m/z}$, was followed continuously using the analogue output, which was recorded by setting up a gate around the m/z peak of interest (normally m/z 23 and m/z 39, corresponding to Na^+ and NaO^+,

respectively) with the scope built-in boxcar function. After data acquisition, the reference measurements were linearly interpolated to the specific measurement times, and the interpolated references were used to correct the measurements taken when the reactant was present. Integration of the digital spectral peaks was performed after acquisition and then the integrated count rates were normalised to the corresponding reference values as well. The processed data were then plotted against the concentration of reagent and fitted using an analytical expression (e.g. an exponential decay for pseudo-first order conditions, see below).

Materials

Reactant gas mixtures were prepared on all-glass vacuum lines. The carrier and diluting gas N_2 (OFN, BOC) was purified using a molecular sieve trap submerged in a bath of liquid nitrogen. N_2O (BOC) and CO_2 (BOC) were frozen in a liquid nitrogen bath and pumped upon for a few minutes before degasing into glass bulbs for dilution. De-ionised H_2O was degassed by pumping over several minutes. H_2 (BOC) was left open to a liquid N_2 bath for a few minutes to remove hydrocarbon impurities. CO (BOC) was used without further purification. An iron rod (Alfa Aesar, 5 mm diameter, 99.99%) was fixed in a rotary feed-through and ablated at 10 Hz by t a frequency-doubled Ng:YAG laser in order to produce pulses of Fe atoms (in this operation mode the ToF-MS skimmer cone is biased positive to repel Fe^+ ions formed in the ablation process). Sodium pieces (Alfa Aesar, 3-12 mm, 99.95%, metal basis) packed in mineral oil were washed with chloroform and sliced into smaller pieces before packing them into the oven.

3. Theoretical methods

In the present study we have used the Master Equation Solver for Multi-Energy well Reactions (MESMER)[38, 39] to extrapolate the experimental rate coefficients to the pressure and temperature ranges relevant to planetary upper atmospheres. A pre-requisite for these calculations is the availability of molecular parameters of the species of interest (rotational constants, vibrational frequencies, anharmonicity constants, dipole moments, polarizabilites and ionisation energies) as well as an accurate potential energy surface (PES) of the reaction. Molecular parameters of the relevant species at B3LYP/6-311+g(2d,p) level (Tables S2 and S3) have been calculated using the Gaussian 09 package.[40] The zero point corrected energies at 0 K of the stationary points in the PES of interest are obtained using the complete basis set extrapolation composite models CBS-QB3 and W1U (total energies are listed in Table S4). Enthalpies of reaction are listed in Table S5.

The master equation solver MESMER groups the ro-vibrational energy levels in the ab initio PES into energy grains. The population in each of these grains (size $=100$ cm^{-1}) is described by a set of coupled differential equations that account for collisional energy transfer and dissociation. Microcanonical rate coefficients for the unimolecular reactions that occur in each energy grain are calculated from the ab initio molecular parameters. The Inverse Laplace Transform method[41, 42] is applied to calculate microcanonical association rates from an estimate of the high pressure limiting rate coefficient for association, which here we set to the capture rate coefficient resulting from long range dipole-dipole, dipole-induced dipole and/or dispersion attractive potentials (Table S6).[11, 43-45] The microcanonical dissociation rate coefficients are then determined by detailed balance. The exponential down model is used for describing collisional energy transfer probabilities. The energy transfer parameter ΔE_{down} is commonly set as adjustable in order to obtain the best fit to experimental data using a non-linear least squares algorithm. Typical values of ΔE_{down} for N_2 are in the range of 300 - 500 cm^{-1}.[39] As a result of the large dipole moment of sodium-containing molecules such as

NaHCO$_3$, the long range attractive forces between the molecular complexes and the bath gas are enhanced by the dipole they induce in the N$_2$ molecules, which results in enhanced collisional frequencies. Therefore, the Lennard-Jones parameters for the interaction potential between molecular complexes and the bath gas N$_2$ are derived from the coefficients of the dipole-induced dipole attractive potentials (Table S7).[43, 44]

4. Results

4.1. Photo-ionisation

Examples of PI spectra obtained by adding N$_2$O to the carrier flow are shown in Fig. 2. In the whole range of energies used in this study (3.4 eV < E$_{PI}$ < 5.6 eV, or 365 nm > λ > 220 nm), the mass spectra are dominated by the peak progressions Na(Na$_2$O)$_n^+$ and NaO(Na$_2$O)$_n^+$ (n = 0 - 4), with additional peaks corresponding to Na$_2^+$, Na$_2$O$^+$ and (NaO)$_2^+$. Other minor progressions can also be observed (e.g. (Na$_2$O)$_n^+$, n = 2 , 3) at longer accumulation times. Fig. 3 shows the dependence on laser power of the integrated signals (panel 4a), with m/z ≤ 78 peaks showing a quadratic dependence and m/z ≥ 85 peaks showing a linear dependence (i.e. single photon ionisation), consistent with ionisation energies close to the photon energy (3.49 eV) for sodium oxide clusters with 3 or more sodium atoms.[24, 26, 46] Due to the close to threshold ionisation, the observed progressions correspond most likely to parent ions. The observation of Na clusters results in part from the relatively high source Na concentrations required to enable observation of NaO and NaOH by PI-ToF, but also from their high ionisation efficiencies. Interferences of cluster formation with the kinetics of NaO are negligible (see below), since it seems to originate from the minor species Na$_2$O rather than from polymerization of NaO. The kinetics and structures of these sodium oxides will be discussed in a separate publication.[47]

The ionisation energies (IE) at W1U level of different sodium containing species are listed in table S8. The two typical PI energies used in this study were 3.94 eV (315 nm) and 3.49 eV (355 nm), which are below the IE of atomic Na (5.1 eV, or 241.2 nm [48]), Na_2 (4.88 eV, or 253.7 nm [48, 49]), NaO (7.55 eV, or 164.3 nm [50]) and Na_2O (5.06 eV, or 245.2 nm [22]). For both photon energies, the signal observed at m/z 23 in the absence of N_2O, S_{23}^0, was very small, and increased upon addition of N_2O reaching a plateau 2 orders of magnitude larger than the signal in the absence of N_2O (S_{23}^{max}). The rate constant for this growth is in very good agreement with the literature rate constant for the Na + N_2O reaction (see below), which indicates that the observed Na^+ signal results mostly from photo-fragmentation of NaO to $Na^+(^1S_0) + O(^3P)$ (7.9 eV) after absorption of two 315 nm photons (2 × 3.94 eV) or three 355 nm photons (3 × 3.49 eV, see Fig. 3). Alternatively, fragmentation to $Na^+(^1S_0) + O^-(^2P)$ is also accessible with 2 × 3.49 eV. Both at 355 nm and 315 nm, a NaO^+ signal ($S_{23}^{max}/S_{39}^{max} \sim 20$) was observed and showed the same growth with N_2O. Photo-fragmentation dominates over the formation of the parent m/z because NaO^+ is bound by just ~0.3 kJ mol^{-1}, and therefore the energy of 2 × 315 nm photons or 3 × 355 nm photons is respectively at the dissociation threshold and above.[51] The power of the 355 nm beam was ~25 mJ $pulse^{-1}$, i.e. about 3-fold more intense than the 315 nm beam, which explains why signals are comparable for two and three photon ionisation. Note that relatively high laser pulse energies are required in order to counter the short lifetime of the pre-dissociated neutral excited state accessed with the first photon (the photolysis absorption cross section of NaO at 315 nm is ~1 × 10^{-17} cm^2 [13]). For 5.6 eV (220 nm, PI energy ~1 mJ $pulse^{-1}$), which lies above the atomic sodium IE, S_{23}^{max}/S_{23}^0 = 40 is observed (i.e. factor of 2 larger S_{23}^0 compared to 315 nm); this may indicate a contribution to m/z 23 of dissociation followed by ionisation ("ladder switching"[52]). Fragmentation energies of different neutral species potentially related to m/z peaks relevant for this study are listed in table S9.

Addition of H_2 or H_2O results in the removal of NaO (R2 and R3), which can be monitored by the decay of the signal at m/z 23 and m/z 39, both for 315 nm and 355 nm. The concomitant formation of NaOH could only be observed reproducibly at m/z 40 (Fig. 4a) when tuning the laser to the maximum of the NaOH absorption band at ~315 nm.[13, 53] The combination of two 315 nm photons (7.88 eV) is ~0.03 eV above the calculated adiabatic IE of NaOH. The absence of a NaOH signature at m/z 23 and m/z 39 is consistent with fragmentation energies significantly higher than the combined energy of two photons (Table S9). Addition of H_2 and H_2O also results in the growth of new species at m/z 63 and 103 (Fig. 4b and 4c), tentatively identified as photo-fragmentation products of the NaOH dimer and trimer, which will be discussed elsewhere.[47]

Finally, the simultaneous addition of H_2O/H_2 and N_2O to the carrier flow upstream of the oven results in a high concentration of NaOH, which is then removed by downstream injection of CO_2 forming $NaHCO_3$ via R4. While removal of NaOH by CO_2 could be followed at m/z 40, the signature of the expected product at m/z 84 was not observed at any PI wavelength, including 220 nm, for which the $NaHCO_3$ UV absorption band peaks.[13] The source chemistry generates high signals at m/z 23 and m/z 39 which do not change upon addition of CO_2. None of the peaks observed in these experiments shows kinetic growth with increasing CO_2.

4.2. Kinetic analysis

For a generic reaction of the form NaX + R $\rightarrow$ NaY + P (Y = O, OH, HCO_3), under pseudo-first order conditions ([R] >> [NaX]) and in the absence of NaX recycling reactions, NaX decreases exponentially with increasing t_{eff} and [R]:

$$\frac{S_R^t}{S_0^t} = \frac{[NaX]_R^t}{[NaX]_0^t} = \exp(-(k \times t_{eff}) \times [R]) \tag{E2}$$

where k is the bimolecular rate constant, and $[NaX]_R^t$ and $[NaX]_0^t$ are respectively the NaX concentrations with and without reactant. S_R^t and S_0^t are the corresponding MS signals, proportional to concentrations. By fitting an exponential function to the plot of observed S_R^t/S_0^t vs [R], the value of $(k \times t_{eff})$ can be obtained. In addition, under pseudo-first order conditions a rate constant can be determined from the growth of the reaction product:

$$[NaY]_R^t \propto S_R^t = A \times (1\text{-}\exp(\text{-}(k \times t_{eff}) \times [R])) \qquad \text{(E3)}$$

where $A = C \times [NaX]_0 \times (1\text{-}\alpha)$ encompasses the proportionality constant C between signal and concentration, the initial concentration $[NaX]_0$ and the branching ratio of the channel producing NaY $(1\text{-}\alpha)$. The contact time t between the reactant and the species of interest can be calculated by dividing the injection distance to the sampling point over the linear speed of the flow (E1), and applying the parabolic velocity profile correction factor of 1.6. It must be noted, however, that off-axis injection of reactant is required in order to minimise deposition of Na-containing species on the injector outer wall and to avoid disrupting the laminar flow. This introduces a mixing time t_0 of the reactant into the flow, meaning that the effective contact time t_{eff} is shorter than the contact time t estimated from the linear speed at the core of the laminar flow. Under pseudo first-order conditions for a reaction with rate constant k and in the absence of secondary chemistry, this mixing time accounts for the intercept of the linear regression of the $(k \times t_{eff})$ vs. t scatter plot, where $(k \times t_{eff})$ is the minor reactant's exponential decay constant (E2 and E3) for a particular contact time t:

$$(k \times t_{eff}) = k \times t + y_0 \qquad \text{(E4)}$$

In E4 y_0 is the loss rate intercept (a negative value). The x value of the intersection between the regression line and the time axis gives the mixing time t_0. From E4 the reaction rate constant k can be determined by linear regression. In most cases, to calculate the rate constant

k it is sufficient to divide the observed ($k \times t_{eff}$) by the calculated t, and then apply a mixing time correction t_0 if necessary:

$$k = (k \times t_{eff}) / (t - t_0) \hspace{4cm} \text{(E5)}$$

In order to estimate t_0, resonance absorption was used to measure the established rate constant for R7. [54-57] In these experiments the absorption of Na at 589 nm was monitored as a function of N_2O injection point (i.e. contact time). Fig. S1b shows that the expected decay rate of Na was reached after ~0.8 ms. This is significantly smaller than would be expected from molecular diffusion (~1.7 ms at 1 Torr N_2 using $D_{Na,N2} = 6.08 \times 10^{-3}\ T^{1.79}\ cm^2\ s^{-1}$ Torr [58]), which suggests that a small amount of turbulence at the injection point facilitates mixing. On the other hand, this small amount of turbulence does not perturb the laminar flow conditions for long. The Fe pulsed source experiments show that the typical injection of 100 sccm of gas through the sliding injector delays the arrival time by less than 3%.

4.3. Reaction of Na and Na_2 with N_2O

The performance of the system was first tested by revisiting the kinetics of the reaction between Na and N_2O. Fig. 5 shows an example of these experiments. The growth of NaO with increasing N_2O was simultaneously observed in the m/z 23 and m/z 39 integrated signals. The large NaO fragmentation signal saturates the m/z 23 peak in counting mode, but it is always possible to monitor it by integrating the analogue peak in the scope as shown in Fig. 5a. Fig. 5b shows that the NaO^+ parent ion grows essentially at the same rate as the Na^+ fragment. From these experiments at different contact times, the rate constant at 295 K was found to be $k_7 = (1.2 \pm 0.5) \times 10^{-12}\ cm^3\ molecule^{-1}\ s^{-1}$, in excellent agreement with the recommended value.[59] The rate constants were determined by averaging the growth constant fitted to the S_{23} and S_{39} experimental curves, and then correcting for the mixing time

determined using the atomic absorption system before applying E5 (~10% correction of k). The quoted uncertainty (2σ) encompasses the statistical error derived from the weighted least squares fits to E3, the uncertainty in [N_2O] and the uncertainty in the contact time (E1) and the mixing time as determined from the absorption measurements (Fig. S1). Some experiments were carried out at higher temperatures (Table 1) by injecting N_2O closer to the oven source and increasing the temperature of the oven itself. The excellent agreement with the recommended rate constant at room temperature[59] rules out a large interference of the NaO self-recombination.

For shorter contact times and lower [N_2O] it was also possible to study the kinetics of the reaction between Na_2 and N_2O:

$$Na_2 + N_2O \rightarrow Na_2O + N_2 \qquad (\Delta H_f = -260.1 \text{ kJ mol}^{-1}) \qquad \qquad \text{(R8)}$$
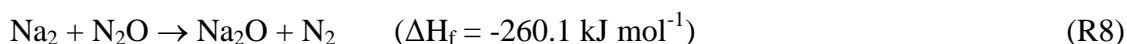
Fig.6 shows that the decay of S_{46} is well matched by the growth of S_{62}, which indicates that the Na_2 released from the source (~2% of the Na concentration at the temperature of the oven, ~650 K) is indeed converted into Na_2O via R8. Note that S_{62} is not zero in the absence of N_2O, which is accounted for by fitting an additive constant with E3. This and other weak signals can be observed straight from the oven without adding N_2O and are related to oxidation of the sodium pellets during the loading of the oven. However, in the short contact time/low [N_2O] conditions of these experiments only S_{46} and S_{62} show variation with [N_2O]. The rate constant determined for R8 at 300 K from the S_{46} decays and S_{62} growths recorded in four experiments using E5 is $k_8 = (1.3 \pm 0.5) \times 10^{-11}$ cm^3 molecule^{-1} s^{-1}.

4.4. Reaction of NaO with H_2O, H_2 and CO

For the kinetic study of R2, R3 and R6, N_2O was added to the N_2 carrier flow to ensure that the Na vapor was converted to NaO within ~1-2 ms after the oven port. The reagents H_2O, H_2

or CO were added at different distances from the sampling skimmer using the sliding injector. For each excess reactant gas, experiments were carried out at different injection distances to the detection point (i.e. contact times) and for each of these injection distances the concentration of sodium-containing reactants and products was monitored as a function of excess reactant concentration.

Figure 7 shows the results obtained for R2. In the upper panel (Fig. 7a) the exponential decay of NaO at m/z 39 (and also at m/z 23, not shown) in the presence of water matches well the growth (E3) of NaOH at m/z 40. The decay/growth rates obtained from the fit of the experimental data depend linearly on the contact time calculated using E1 (Fig. 7b). Linear regression (E4) yields a value of the rate constant of R2 at 310 K of $k_2 = (2.4 \pm 0.6) \times 10^{-10}$ cm^3 $molecule^{-1}$ s^{-1}. The crossing point of the fitted line with the x axis is consistent with the mixing time of 0.8 ms derived from atomic absorption measurements. The linear dependence of decay rates on contact time supports a marginal interference of second order processes such as NaO + NaO.

For the study of R3, numerical modelling and fitting of the experimental data was initially carried out in order to allow for the recycling of Na via R3b and subsequent reformation of NaO via R7. However, the results obtained using this approach indicated a small branching ratio for channel R3b, and therefore the same analytic approach used for R2 was adopted for R3, i.e. it was assumed that R3a is the dominant channel and E2 and E3 were used, respectively, to fit the NaO decay and NaOH growth in the presence of H_2 (Fig. 8a). The rate constant of R3 at 310 K obtained from the linear fit in Fig. 8b (E4) is $k_3 = (4.9 \pm 1.2) \times 10^{-11}$ cm^3 $molecule^{-1}$ s^{-1}. A temperature dependence of the rate constant cannot be discerned from the determination at 266 K, which overlaps the value at 310 K within the 2σ error bar.

Additional experiments were carried out to establish the product branching ratio of R3, by looking at the two products of the reaction. First, the enhancement in Na resonance absorption by addition of H_2 was measured (Fig. 9b, red squares), and this was modelled numerically by integrating the set of differential equations resulting from R3, R7 and the diffusional loss of Na and NaO.[14, 60] The rate constant for R7 at 350 K was taken from the literature[55] and the rate constant of R3a was fixed at the value obtained from the analysis described in the previous paragraph. The H_2 mixing time is taken into account by using a 0.8 ms long linear H_2 injection function. A non-linear least squares algorithm was employed to find the rate constant for R3b that produces the best fit between the observed and simulated [Na] vs [H_2] curve (Fig. 9b). Fig. 9a shows two examples of concentration vs. residence (contact) time curves in the absence of H_2 (thin lines) and for the maximum H_2 concentration employed (thick lines), where the last value of each of the [Na] vs. t curves corresponds to the modelled Na concentration at the observation point, which is shown in Fig. 9b as a function of [H_2]. From this modelling exercise, a value of $\alpha = (0.028 \pm 0.014)$ % (2σ) is obtained. A second set of experiments was carried out where the NaOH signal (S_{40}) was monitored by adding H_2 and H_2O back-to-back at the same injection point (Fig. 9c). The concentrations of H_2 and H_2O added were such that they produced similar growth rates of NaOH and resulted in complete reaction in both cases, as shown by the modelled curves in Fig. 9c. From E3, it follows that at large H_2 and H_2O:

$$S_{40}^{H_2}/S_{40}^{H_2O}=[\text{NaOH}]_{40}^{H_2}/[\text{NaOH}]_{40}^{H_2O} \cong (1\text{-}\alpha) \qquad\qquad (E6)$$

Figure 9c shows that within uncertainty the signal obtained from both reactions is identical. Using the average of the four data points obtained for each reagent, a branching ratio of (1-α) = (1.02 ± 0.14) % is obtained from E6. This implies an upper limit of $\alpha < 0.12$, consistent with the Na resonance absorption measurements.

The reaction NaO + CO (R6) was investigated using the same approach described above. Fig. 10a shows several decays of NaO in the presence of increasing [CO]. It can be seen that NaO decays to a non-zero baseline, which is a consequence of Na being the only product of R6. Na then goes on to react with N_2O rapidly (since the N_2O is in high excess) to reform NaO via R7. Integration of the set of differential equations describing R6, R7 and diffusional loss of Na and NaO results in the following expression:

$$S_{23} = A\frac{k_7[N_2O] + k_6[CO]\,e^{-(k_7[N_2O]+k_6[CO])t}}{k_7[N_2O]+k_6[CO]} + B \qquad\qquad (E7)$$

This expression is derived by assuming that the diffusion coefficients for Na and NaO are similar, as has been shown previously.[14, 60] The constant A encompasses the diffusion factor and the scaling between signal and concentration, while B accounts for potential fragmentation of other species yielding signal at m/z 23. This expression was fitted to the experimental data in Fig. 10a by floating the rate constant k_6 and fixing the value of k_7 to the literature value, which is essentially in agreement with the determination in this work (section 3.2). The calculated contact time and the measured concentration of [N_2O] are prescribed and the additive factor B was constrained to be larger or equal than zero. The weighted average of eight determinations at different contact time (Fig. 10b) yields a value for the rate constant of $k_6(300\ K) = (1.2 \pm 0.4) \times 10^{-10}\ cm^3\ molecule^{-1}\ s^{-1}$ (2σ). This value includes a correction for the CO flow mixing time. The S_{39} decays have not been considered in the determination of k_6 because the data are generally noisier than for S_{23} (these experiments were run at lower oven temperatures, ∼ 620 K), although the analysis of S_{39} yielded the same decay rates are within error. Numerical simulations considering R6, R7 and the diffusional losses of Na and NaO were carried out to estimate the uncertainty which arises from using E7 with the assumption that Na and NaO have the same diffusion coefficient. The diffusion coefficient of Na

measured by Silver[58] results in a radial diffusion rate of 364 s^{-1} at 1 Torr and 300K,[29] while the diffusion coefficient reported by Cox et al.[14] for NaO yields a 15% smaller diffusional loss rate for NaO. The average optimal value of k_6 to fit the simulated NaO curves to the experimental NaO decays was found to be $k_6(300 \text{ K}) = (1.1 \pm 0.2) \times 10^{-10} \text{ cm}^3 \text{ molecule}^{-1} \text{ s}^{-1}$, within the error bar of the analytical determination.

4.5. Reaction of NaOH with CO_2

The reaction between NaOH and CO_2 (R4) was studied by adding N_2O and H_2O or H_2 to the carrier gas and flowing CO_2 through the sliding injector. All experiments were conducted at approximately the same contact time (~5 ms) by balancing pressure and carrier flow. While an excellent detection of NaOH was achieved at m/z 40 by using 315 nm PI, no sign of the product of R4, $NaHCO_3$, was observed at m/z 84 for any PI wavelength. Fig. 11a shows NaOH decays (S_{40}) for 3 different pressures at 305 K fitted to E2. The bimolecular rate constant was determined using E5. Additionally, a measurement at 2 Torr was carried out at a temperature of 266 K. The bimolecular rate constants obtained at 4 different pressures and 2 different temperatures are summarised in Table 1 and in Fig. 11b. Assuming that the reaction was in the low pressure limit,[17] a linear fit to the data would yield the following low pressure limit rate constant: be $k_{4,0}(305 \text{ K}, P < 4 \text{ Torr}) = (7.6 \pm 1.6) \times 10^{-29} \text{ cm}^6 \text{ molecule}^{-2} \text{ s}^{-1}$ (2σ).
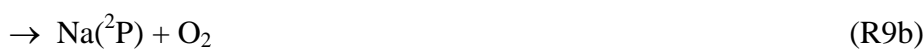
5. Discussion

5.1. NaO reactions with H_2O, H_2 and CO.

The exothermicity of the Na + N_2O reaction (R7) enables NaO to be generated both in the $A^2\Sigma$ and $X^2\Pi$ states, which are separated by ~ 23.93 kJ mol^{-1} (0.25 eV).[61] The lifetime of the A state has been estimated to be longer than 10-30 ms,[61] which may be relatively long compared to the reaction time in pulsed laser photolysis (PLP) experiments, but comparable

with flow tube residence times. There is some evidence that collisional relaxation may also affect the relative population of states on typical experimental time scales. According to the band assignment in the photoelectron spectra recorded by Wright et al.,[51, 62] a large fraction of NaO is generated in the A state (at least 4:1 according to band intensity ratios), which is similar to the close to 1 branching ratio of the A state channel in the $Na + O_3$ reaction.[63] Wright et al. reported evidence of a variable A:X population ratio from both the $Na + N_2O$ and $Na + O_3$ reactions. This supports the idea of a large A state branching ratio for R7 with most of the X state observed resulting from collisional deactivation. Moreover, Joo et al.[61] observed collisional quenching of the A state by the He/Ar bath gas in their flow tube experiment at 1-3 Torr, based on enhancement of the $NaO(X^2\Pi) \rightarrow NaO(A^2\Sigma)$ absorption about 3 - 8 ms downstream of the source region, either by increasing pressure or by increasing the residence time a few milliseconds. Finally, recent studies of the dependence of the sodium D line ratio on oxygen concentration support efficient quenching of NaO(A) by O_2.[64] Therefore, the different rate constants reported in the literature measured using R7 as a source of NaO are likely to correspond to a range of mixtures of both NaO states, where the relative population of states depends on pressure, bath gas, and residence time in the reactor. This requires some consideration when comparing rate constants measured under different experimental conditions and detection schemes, and constitutes also a potential source of systematic error when using NaO laboratory rate constants in atmospheric modelling, keeping in mind that under mesospheric conditions a different range of steady-state relative populations of the A and X states are likely to be found.[64]

The rate constant for the $NaO + H_2O$ reaction (R2) determined in this study is in very good agreement with a previous determination by Ager and Howard,[11] $k_2(298K) = (2.2 \pm 0.4) \times 10^{-10}$ cm^3 $molecule^{-1}$ s^{-1}, who used a similar flow tube configuration at slightly lower He or N_2 pressure (P ≤ 0.5 Torr) and a comparable range of reaction times. However, a previous

study by Cox and Plane[12] using a PLP-chemiluminescence arrangement at 10 Torr N_2 obtained a value ~3 times lower, in contrast to the good agreement between the flow tube and PLP techniques for the $NaO + O_3$ reaction.[56, 65] The glass lines and mixing methods used in the present study are the same as those used by Cox and Plane, yet we obtain the same result as Ager and Howard which indicates that errors in the H_2O concentrations are an unlikely explanation.[12] A different reactivity of the A and X states of NaO with H_2O could be an explanation for the disagreement. Regarding detection, all three studies are insensitive to the state of NaO. In particular, the Cox and Plane study relies on residual N_2O photolysis at 193 nm to generate atomic oxygen, which further reacts with NaO to produce $Na(^2P)$ chemiluminescence, thereby providing a marker to track the NaO concentration:

$$NaO(X^2\Pi) + O(^3P) \rightarrow Na(^2S) + O_2 \qquad\qquad (R9a)$$

$$\rightarrow Na(^2P) + O_2 \qquad\qquad (R9b)$$

$$NaO(A^2\Sigma) + O(^3P) \rightarrow Na(^2S) + O_2 \qquad\qquad (R10a)$$

$$\rightarrow Na(^2P) + O_2 \qquad\qquad (R10b)$$

The current understanding of R9 and R10 is that they produce $Na(^2P)$ with the same efficiency ($f \sim 0.17$),[64, 66] and therefore $Na(^2P)$ chemiluminescence was a marker for the mixture of NaO states in Cox and Plane's study. However, as mentioned above, state selectivity can also be achieved by relaxation, i.e., the rate constant of $NaO(X) + H_2O$ would have been measured after a long residence time in the flow tube as a result of quenching and radiative relaxation, while the slower rate constant measured in the PLP experiment would have been measured in an NaO(A) state rich mixture. We obtained some evidence of this behavior in the present experiments by injecting water very close to the section of the flow

tube where NaO is produced. Fig. S2 shows that the decay of S_{39} with increasing [H_2O] is slower when H_2O is injected 0.6 ms downstream of the source, compared to injection 15 ms downstream. Such behaviour was mirrored by all sodium oxide signals at m/z > 39 and also by the m/z 23 fragment. We did not attempt to measure rate constants at these long contact times due to the difficulty in regulating the temperature in the reaction zone and the low S_{39} signal caused by diffusion. Finally, note that the good agreement between the analogous flow tube[56, 67] and PLP-LIF[65] measurements for $NaO + O_3$ is facilitated by the presence of O_2, which quenches efficiently $NaO(A^2\Sigma)$ to $NaO(X^2\Pi)$ with a rate constant of $\sim 1 \times 10^{-11}$ cm^3 molecule^{-1} s^{-1} due to near-resonance electronic-vibrational energy transfer. [61, 65]

Some radiative relaxation of the A state in the flow tube experiments cannot be excluded. Calculations by Langhoff reported by Joo et al.[61] suggest lifetimes longer than 20 ms. Assuming that relaxation plays a minor role in our flow tube system (~15 ms residence time), a rough estimate of the quenching rate by N_2 can be attempted by comparing to the kinetics of chemiluminescence in the PLP experiment. The quenching rate needs to be at least 300 s^{-1} to relax all the A state in the flow tube experiment prior to detection, which results in a lower limit for the quenching rate constant of $\sim 1 \times 10^{-14}$ cm^3 molecule^{-1} s^{-1}. In Cox and Plane's experiments at 10 Torr, this would correspond to a quenching rate of 3000 s^{-1}, which would have had made their experiment sensitive only to $NaO(A^2\Sigma)$ with a small impact on the observed kinetics (see Supplementary Information).

With this background, the RRKM treatment of R2 by Cox and Plane needs to be revisited. We have first recalculated the PES at CBS-QB3 level and found that the energetics of the reaction are in essence the same that they reported at the CBS-Q level of theory. The reaction is thermoneutral (+0.6 kJ mol^{-1} at 0 K), although, in contrast to the HF treatment of the transition state between the two $NaOH_2$ isomers by Cox and Plane, the CBS-QB3 model

yields a negligible energy difference, which is also shown by intrinsic reaction coordinate (IRC) calculations.[40] We assume first the high pressure limit for the ILT approach to be equal to the rate constant calculated by Stoecklin and Clary, resulting from the adiabatic capture partial centrifugal sudden approximation treatment of the dipole-dipole interaction potential between NaO (μ = 7.9 D) and H_2O (μ = 1.8 D). Lennard-Jones parameters of the interaction potential between the adduct and the bath gas are calculated from the dipole-induced dipole interaction potential between the NaO_2H_2 ($\mu \sim$ 5.8 D) and the bath gas molecule N_2 (σ = 4.0 Å and ε = 420 K).[44] The results of these calculations (Fig. S4) are in good agreement with the value of k_2 at 310 K reported here without adjusting the enthalpy of reaction. This is in contrast to the RRKM modelling carried out by Cox and Plane, who had to increase ΔH_r^0 to +4.3 kJ mol^{-1} (note that this is within the experimental uncertainty) to match the room temperature rate constant and the observed Arrhenius behaviour. As shown in Fig. S4, the modelled rate constants are very sensitive to this parameter, as well as to the high pressure limit rate constant assumed.[44, 45] Two recent ab initio studies at CCSD(T)//CBS [68] and WnC [69] level reporting the NaO and NaOH enthalpies of formation indicate that the reaction is exothermic by just 2 kJ mol^{-1} at 298 K (thermoneutral at 0 K), with an estimated accuracy of $\pm$3 kJ mol^{-1}. On the other hand, NaO(A$^2\Sigma$) + H_2O is exothermic by ~24 kJ mol^{-1}, so a marked temperature dependence such as the one they observed is in principle difficult to reconcile with their measurements being characteristic of an A-state rich mixture.

It could be argued that temperature dependent wall losses of water associated to a highly hygroscopic sodium hydroxide wall coating could have affected the Cox and Plane determination, in such a way that at low temperature the H_2O concentration would have been effectively lower than calculated from pressure and flow readings, causing the apparent Arrhenius behaviour observed. However, given the number of uncertainties involved in the discussion above, we cannot currently identify the most likely cause of experimental

disagreement. Future state-selective measurements of k_2 and of the uncertain NaO and NaOH enthalpies of formation are needed, but based on the discussion above about NaO($A^2\Sigma$) relaxation and on current ab initio estimates of the enthalpy of reaction, we recommend a weighted average of the value reported here and Ager and Howard's for the rate constant of NaO(X) + H_2O, k_2(300 K – 310 K) = (2.3 ± 0.5) × 10^{-10} cm^3 molecule^{-1} s^{-1}, with an Arrhenius temperature dependence determined by an activation energy of 2 kJ mol^{-1}:

$$k_2(T)=5.06 \times 10^{-10} \exp(-240/T) \text{ cm}^3 \text{ molecule}^{-1} \text{ s}^{-1} \tag{E8}$$

Only one previous determination of R3 has been reported in the literature, obtained by Ager and Howard with a flow tube apparatus.[11] This is a factor of ~5 faster than the value found in the present study from the direct NaO decay and the NaOH growth. Such disagreement is unexpected considering the excellent agreement for R2. From the discussion above the cause of the discrepancy is unlikely to be a different population and reactivity of the A state. As in the measurement of k_2, Ager and Howard relied on chemical conversion of NaO(X) to Na(^{2}P) with contact times very similar to the ones considered in the present study. Numerical modelling of their experiments, including the chemical conversion scheme, is straightforward and shows that their assumptions and data analysis are sound. Interference from substantial Na recycling (R3b) would have affected both determinations of k_3 in the same way, and we have now shown by looking at the two accessible product channels that the branching ratio for Na production is very small. In our PI-ToF-MS measurements, fragmentation of larger species could have caused interference in the masses followed during kinetic experiments, but this appears unlikely considering that the same kinetics are obtained from the decay of the Na$^+$ fragment and the NaO$^+$ parent mass, as well as from the growth of the NaOH$^+$ product parent mass.

In either case, k_3 is 1-2 orders of magnitude slower than the collision rate constant and the dipole-induced dipole capture rate constants.[11, 43, 45] This is remarkable considering no barriers are found in either of the two product channels (Fig. S5a). Intrinsic reaction coordinate (IRC)[40] calculations at the B3LYP/6-311-G+(2d,p) level show that the transition state connects a very shallow NaO…H_2 entrance complex to a Na…OH_2 complex, which is weakly bound with respect to channel R3b products. Note that according to our observations R3b is very minor compared to R3a. On the other hand, classical trajectory calculations using the Atom Centred Density Matrix Propagation (ADMP) molecular dynamics model[40] show that whenever a collision at thermal energies is reactive, it forms R3a products (Fig. S6), although only collisions with a small impact parameter are reactive. At this stage theoretical considerations do not shed light into the reaction mechanism, possibly because a more advanced multi-reference method is required. The reason why the overall rate constant is slow also remains unclear. This reaction is challenging from a theoretical point of view and probably worth a molecular dynamics study.

The rate constant of the NaO + CO reaction does not appear to have been determined before. The reaction proceeds essentially at the hard-sphere collision rate constant. Although the dipole- dipole interaction is weak owing to the small dipole moment of CO (0.11 D), the dipole-induced dipole capture rate constant is a factor of 5 times larger than the measured rate constant. The PES of the reaction (Fig. S5) is rather simple, showing a ring complex bound by 279 kJ mol^{-1} with respect to the reactants, and separated from an exit complex by a 40 kJ mol^{-1} transition state at CBS-QB3 level. The exit complex is only ~6 kJ mol^{-1} bound with respect to the products.

We have not studied experimentally the rate constant of NaO + CO_2 (R5) in the course of this work. Only one previous determination of k_5 has been published previously,[70] which shows

that the reaction is in the fall-off region between 0.2 and 1.5 Torr. For completeness we have performed master equation calculations on this reaction, which are described in the following section alongside the results for the $NaOH + CO_2$ reaction.

5.2. $NaOH + CO_2$ and $NaO + CO_2$

The reaction between NaOH and CO_2 (R4) studied previously at room temperature by Ager and Howard,[17] who observed third order behaviour in the 0.4 – 1.5 Torr pressure range and derived a low pressure limit rate constant of $k_{0,4}$ (298 K) = (1.3 ± 0.3) × 10^{-28} cm^6 $molecule^{-2}$ s^{-1} for N_2. In their experiments high N_2O mole fractions were used, which were varied between ~0.15 and 0.55 in order to disentangle the third body contributions of N_2O and N_2. In our case the molar fraction of N_2O used was significantly lower (~0.03), which enabled us to ignore its third body effect. Our data (1 - 4 Torr) is also compatible with third-order behaviour within uncertainty (Fig. 11), although we derive an apparent low pressure limit rate constant a factor of ~2 lower: $k_{0,4}$ (298 K) = (7.6 ± 1.6) × 10^{-29} cm^6 $molecule^{-2}$ s^{-1}. Again the reason for discrepancy is unclear, although in this case the error bar of our bimolecular rate constant at 1 Torr overlaps within the uncertainty range of Ager and Howard's rate constant at the same pressure after correcting for the contribution of N_2O (Fig. 11), and the disagreement results mostly from their measurement at 1.5 Torr.

The results of master equation calculations shown in Fig. 11 indicate that the reaction is actually well within the fall-off region at 0.4 Torr and above, which implies that the slope of the k vs P plot underestimates the true third-order rate constant. In these calculations, the well depths and barrier heights are fixed at the CBS-QB3 values (see Fig. S6 and Table S5; values at the WU1 level of theory agree within 2 kJ mol^{-1}). To estimate the high pressure limiting rate constant required in the ILT formulation of the RRKM expression, we have considered the largest contributing term to the capture rate constant in the μJ-VTST formulation by

Georgievskii and Klippenstein (Table S6), multiplied by 1.3 to correct for other contributions to the attractive potential, which cannot be accounted for simply by addition of terms.[44] For collisions of the $NaHCO_3$ adducts with the bath gas, the Lennard-Jones potential parameters σ (centre of mass distance, in Å) and ε/k (potential amplitude in K) are chosen so that the Lennard-Jones collision rate constant matches the μJ-VTST capture rate constant, which is unusually large due to the high dipole moment of NaOH and the polarizability of CO_2. The value of σ should be approximately equal to a volume-averaged geometric value of ~4.5 Å for $NaHCO_3$ + N_2.[71] Thus, we have chosen to keep this value fixed and increase ε/k until the aforementioned rate constants match, resulting in ε/k = 350 K for $NaHCO_3$ + N_2. Finally, MESMER was run in order to fit the observed bimolecular rate constants by floating the value of the energy transfer parameter ΔE_{down} at 300 K, while a temperature dependence of this parameter of $T^{0.6}$ was assumed (Fig. S7). The optimal value of $\Delta E_{down}(300 \text{ K})$ = (550 ± 170) cm^{-1} is relatively large compared to typical values for N_2 collisions,[39] but the parameter uncertainty is also large and encompasses the high range of typical values for N_2. Note that in order to match Ager and Howard's rate constants with the master equation model an unrealistically high value of ΔE_{down} is required (~700 cm^{-1}). The satisfactory fit of MESMER to the experimental data from the present study can then be used to extrapolate the rate constant to atmospherically relevant conditions, yielding (see the lower panel of Fig. S7 for further details):

$$k_{0,4} (N_2, 193 \text{ K} - 333 \text{ K}) = 2.3 \times 10^{-28}(T/300)^{-4.12} \text{ cm}^6 \text{ molecule}^{-2} \text{ s}^{-1} \quad \text{(E9)}$$

The low pressure limiting rate constant at 300 K is 1.8 times larger than the value reported by Ager and Howard. The rate expression E9 is applicable for all conditions relevant in the upper atmosphere above 80 km (P < 7.5 mTorr) and has important implications for the modelling of the Earth's sodium layer.

Hildenbrand and Lau[72] performed a mass spectrometric search of $NaHCO_3$ using a high temperature (T = 1165 K) effusion cell source containing solid NaOH, through which a flow of CO_2 was passed. They did not observe any parent or fragment ion species associated with $NaHCO_3$, which they attributed to thermal decomposition of this molecule. From an upper limit of the $NaHCO_3$ partial pressure in their system, estimated from the detection limit of their mass spectrometer, they derived a lower limit for the equilibrium constant of R4, and from this a lower limit to the enthalpy of reaction at 298 K of R4 of -121 ± 21 kJ mol^{-1}, which is compatible with our calculated value of -133 kJ mol^{-1} at the W1U level considering the experimental uncertainty. Under the experimental conditions of our study (T ~ 300 K), $NaHCO_3$ is stable and the MESMER simulations show that only a negligible fraction of $NaHCO_3$ would fall apart to produce a NaOH signal. From this we conclude that the lack of $NaHCO_3$ signatures is due to detection constraints, e.g. the absence of a neutral excited state which could assist 3×355 nm PI as for NaO, and the low single photon absorption cross section at 220 nm.[13]

An analogous master equation modelling exercise can be carried out for the reaction between NaO and CO_2 (R5) using the experimental data of Ager and Howard.[70] We followed the same approach for estimating the high pressure limit rate constant of R5 and the appropriate Lennard-Jones parameters for the $NaCO_3 + N_2$ collision, for which setting $\sigma = 4.5$ Å results in $\varepsilon/k = 400$ K. For fitting Ager and Howard's dataset over the whole range of pressures reported (not only the third-order regime, for which bath gas specific values were reported), the effect of the substantial N_2O molar fraction present in their experiments needs to be considered. The observed bimolecular rate constants plotted in their paper correspond to a 0.25 molar fraction of N_2O, which results in a weighted average of $\varepsilon/k = 420$ K for the bath gas mixture. The optimal value obtained from the fit of MESMER simulations to this dataset is $\Delta E_{down}(300 \text{ K}) = (647 \pm 100)$ cm^{-1}, which is again rather large. The uncertainty range

overlaps with the optimal value determined for the NaOH + CO_2 reaction and in fact, Fig. S8 shows that using ΔE_{down}(300 K) = 550 cm^{-1} as a fixed parameter does not result in a poor mismatch between simulated and experimental data. It may be argued that the larger optimal ΔE_{down} results from a larger energy transfer efficiency of collisions with N_2O, which is not considered in the model, or simply that Ager and Howard's observed bimolecular rate constants for R5 are too high as appears to be the case for R4, although perhaps the problem lies only in the chemical conversion method employed for R4 using hydrogen atoms, given the good agreement for NaO + H_2O.

For the modelling of atmospherically relevant rate constants of R5 we have run MESMER for N_2 bath gas and used the same value of ΔE_{down}(300 K) = 550 cm^{-1} as for R4, resulting in the following expression (see Figure S8 for further details):

$$k_{0,5} (N_2, 193\ K - 333\ K) = 1.2\times10^{-27}(T/300)^{-3.14}\ cm^6\ molecule^{-2}\ s^{-1} \qquad\qquad (E10)$$

Thus, the low pressure limit rate constant is 1.4 times larger than the value derived by Ager and Howard from extrapolation of their two lowest pressure points to zero. Both low pressure limit rate constants $k_{0,4}$(300 K) and $k_{0,5}$(300 K) obtained using our master equation based extrapolation method lie outside the uncertainty range of Ager and Howard's values.

5.3. Atmospheric implications

As a result of the aforementioned rapid quenching of NaO(A) by O_2,[64, 73] in the atmosphere the relevant rate constants of NaO reactions are those of the $X^2\Pi$ state. Taking this into account we have updated our 1D atmospheric model of the mesospheric sodium layer (NAMOD) [64, 74] using the rate constants determined in the present study. The bottomside of the neutral Na layer is controlled by R2 and R4, and the consequences of faster rate constants of these reactions are faster removal of Na and formation of $NaHCO_3$. Thus, the salient

feature of this modelling exercise is a narrower modelled Na layer peaking at ~94 km, i.e. ~4 km higher than the LIDAR observations (Fig. 12). This points towards a Na atom recycling process whose rate constant is underestimated or which is not included in NAMOD at all. Inspection of the standard sodium chemical scheme (Table 1 in Plane [74]) shows that a major source of uncertainty is the reaction:

$$NaOH + H \rightarrow Na + H_2O \hspace{3cm} (R11)$$

Of all the neutral sodium reactions considered to be important in the Earth's mesosphere, R11 is the only one for which a rate coefficient at relevant temperatures has not been reported in the literature. A lower limit $k_{11}(300 \text{ K}) > 4 \times 10^{-12}$ cm^3 molecule^{-1} s^{-1} has been published,[10] and extrapolation from high temperature measurements in flames (T = 1800 K − 2200 K) yields $k_{11}(300 \text{ K}) = 1.8 \times 10^{-11}$ cm^3 molecule^{-1} s^{-1}. In NAMOD, the rate constant currently assumed is: $k_{11} = 4 \times 10^{-11}$ exp(-550/T) cm^3 molecule^{-1} s^{-1}, with k_{11} (300 K) = 6.4×10^{-12} cm^3 molecule^{-1} s^{-1}. A rate coefficient of the order of ~5×10^{-11} cm^3 molecule^{-1} s^{-1} would bring the modelled layer into agreement with the observations.

The rate coefficient of the NaO + CO reaction had not been reported previously. The reaction is fast and needs to be included now in schemes for sodium chemistry in the Martian atmosphere. Meteoric ablation in Mars occurs between 75 and 85 km[75] and at this altitude CO is more abundant than O.[76] With the rate constant obtained in this work, the first-order loss rate of NaO by reaction with CO is similar to the removal rates by CO_2 and O (Fig. 13). Since the reaction with CO_2 (R6) is a sink for sodium and the reaction with O recycles atomic sodium, the effect of including the CO reaction is a longer lifetime of the atomic Na layer.

6. Conclusions

A flow-tube apparatus coupled to a photo-ionisation time-of-flight mass spectrometer has proven to be an effective system for studying the gas-phase reactions of atmospherically relevant sodium-containing species at room temperature and below. This setup has allowed the first direct observation of NaO and NaOH at low temperatures using quasi-resonance multiphoton ionisation, facilitating kinetic experiments and the determination of rate constants. Single photon ionisation also enabled the observation of sodium clusters of fundamental interest which had been observed previously only at non-thermal collision energies in cross molecular beam studies. The kinetics and electronic structure of these oxide, hydroxide and carbonate clusters will be discussed in a separate publication.

A new determination of the rate constant of the NaO + H_2O reaction has been reported. The good agreement with the result of a previous flow tube study and disagreement with measurements performed in our laboratory a few years ago using PLP-LIF have been rationalised in terms of population/depopulation of the low lying $A^2\Sigma$ excited state of NaO, which seems to react more slowly with H_2O than the ground state. Our measurement of a rate constant for the NaO ground state reaction is relevant for the atmosphere chemistry of the sodium layer, since in the atmosphere NaO(A) is rapidly quenched by O_2. In addition, we have determined the rate constant of the NaOH + CO_2 reaction as a function of pressure and have extrapolated the results to relevant temperatures and pressures using master equation calculations. Our results indicate that the reaction is in the fall-off region in the typical range of pressures of flow tube experiments, which means that the assumption of low pressure limit in a previous study had resulted in an underestimation of the true third-order rate constant relevant in the upper atmosphere. A similar conclusion can be extracted from the analysis of previously reported data for the NaO + CO_2 reaction, which is important in the Martian

35

atmosphere. Also of relevance for the Martian atmosphere is the first determination of the rate constant of the NaO + CO reaction.

The implementation of the faster rate coefficients of the NaO + H_2O and NaOH + CO_2 reactions in a 1D model of the Earth's sodium layer results in a narrower Na layer peaking at higher altitude then the ground based observations, which highlights a remaining issue in the atmospheric modelling of Na, namely the reaction between NaOH and H. Direct measurements of this rate constant at room temperature and below need to be carried out in order to eliminate this uncertainty from the model. These measurements can be now carried out in our experimental system by direct observation of the NaOH removal by an excess of H atoms.

Acknowledgments

Supporting information available

Figures S1-S8, discussion of the results for the NaO+H_2O reaction by Cox and Plane[12], tabulated ab initio molecular parameters and energies, and long range attraction rate coefficients (Tables S1-S8). This information is available free of charge via the Internet at http://pubs.acs.org.

Tables

Table 1. Summary of rate constants determined in this work with the corresponding experimental conditions.

	Reaction	m/z [a]	T/K	$\Delta T/K$ [b]	P /Torr	k/10^{-12} [c]	Δk /10^{-12} [d]
R7	$Na+N_2O\rightarrow NaO+N_2$	23	295	1	1.3	1.2	0.5
			300	2	2.7	1.5	0.7
			320	10	1	1.7	0.6
R8	$Na_2+N_2O\rightarrow Na_2O+N_2$	46+62	300	2	2.6	13	6
R2	$NaO+H_2O\rightarrow NaOH+OH$	39+40	310	5	1-3.9	240	70
R3	$NaO+H_2\rightarrow NaOH+H$	23+40	266	15	1	6	3
			310	5	1-2.7	4.9	1.2
R6	$NaO+CO\rightarrow Na+CO_2$	23	300	2	2	120	50
R4	$NaOH+CO_2\rightarrow NaHCO_3$	40	266	15	2	8	4
			300	3	1	2.8	2.4
			300	3	2	4.6	2.2
			300	3	3	8	3
			300	3	4	9.7	2.5

[a] Mass to charge ratio of ionised reactant or product [b] Standard deviation of the axial temperature profile. [c] Bimolecular rate constant in cm^3 molecule^{-1} s^{-1}. [d] Uncertainty of rate constants in cm^3 molecule^{-1} s^{-1} at 95% confidence level.

Figure Captions

Figure 1 Schematic of the fast flow tube with the REMPI-TOF-MS detection system. The two available metal sources (furnace and laser ablation) are depicted.

Figure 2. Typical photoionisation spectra obtained by adding N_2O to the carrier flow for 3 PI wavelengths: 355 nm (a), 315 nm (b) and 220 nm (c). The spectra are scaled to the same arbitrary m/z 23 peak signal (note the log scale). The m/z 23 peaks in (a) and (b) have been corrected. The major peak progressions observed are highlighted in panel (a): $Na(Na_2O)_n^+$ in black, $NaO(Na_2O)_n^+$ in red, $Na_2O(Na_2O)_n^+$ in green, and $(NaO)_2(Na_2O)_n^+$ in green (n=0,..,3). Peaks not belonging to the aforementioned progressions are highlighted in panel (b) and include the sodium dimer cation (m/z 46) and a number of peaks (m/z in italics) related to a small air leak and/or oxidation of the Na oven load during preparation: Na_2OH^+ (m/z 63), $Na_3O_2H^+$ (m/z 102) and $Na_3CO_3^+$ (m/z 129). Small peaks related to pump oil appear in panel (b).

Figure 3. Dependence of integrated peak signal ($S_{m/z}$) on laser power (P) for 355 nm PI. Panel (a): exponents of the power law dependence from the log $S_{m/z}$ vs log P linear regressions. Panel (b): experimental[22, 24, 46, 48, 50] IE for the corresponding neutral species.

Figure 4. Spectral proof of NaOH and related species for 315 nm PI wavelength. Panel (a): removal of NaO by H_2O and formation of NaOH (black: low water concentration, black high water concentration). Panel (b): upon addition of water the m/z 62 peak decreases and the m/z 63 peak grows. Panel (c): the same for m/z 101 and m/z 103.

Figure 5. Growth of NaO by addition of N_2O to the carrier flow (R7) via sliding injector (P = 2. 7 Torr, T = 300 K, t = 10 ms) for 355 nm PI wavelength. Panel (a): area under the m/z 23 peak analogue signal vs. $[N_2O]$ (the digital m/z 23 peak is saturated due to the large detection

signal). Panel (b): area under the m/z 39 peak digital signal vs [N_2O]. The experimental data in panels (a) and (b) (squares) is fitted to E3 by non-linear least-squaresto obtain ($k \times t_{eff}$) for R7 (solid line fitted expression, dashed lines confidence bands).

Figure 6. Decay of Na_2 (S_{46}, left axis, black) and growth of Na_2O (S_{62}, right axis, blue) by addition of N_2O (R8) via sliding injector (P = 2. 7 Torr, T = 300 K, t = 8 ms) for 355 nm PI wavelength. The experimental data is fitted to E2 and E3 by non-linear least-squares to obtain ($k \times t_{eff}$) for R8 (solid line fitted expression, dashed lines confidence bands).

Figure 7. Determination of k_2. Panel (a): example of decay of NaO (S_{39}, left axis, black) and growth of NaOH (S_{39}, right axis, blue) by addition of H_2O (R2) (P = 1.0 Torr, T = 310 K, t = 4.4 ms, PI 315 nm). The data is fitted to E2 and E3 by non-linear least-squares to obtain ($k \times t_{eff}$) for R2. Panel (b): Experimental ($k \times t_{eff}$) values vs. calculated contact time t (squares: NaO decays, circles: NaOH decays). The rate constant for R2 is obtained by linear regression of ($k \times t_{eff}$) vs. t.

Figure 8. Determination of k_3. Panel (a): example of decay of NaO (S_{39}, left axis, black) and growth of NaOH (S_{39}, right axis, blue) by addition of H_2 (R3) (P = 1.0 Torr, T = 266 K, t = 6.1 ms, PI 315 nm). The data is fitted to E2 and E3 by non-linear least-squares to obtain ($k \times t_{eff}$) for R3. Panel (b): Experimental ($k \times t_{eff}$) values vs. calculated contact time t (squares: NaO decays, circles: NaOH decays; black symbols: 310 K, red symbols: 266 K). The rate constant for R3 at 310 K is obtained by linear regression of ($k \times t_{eff}$) vs. t.

Figure 9. Determination of the branching ratio of R3. Panel (a): Modelled concentration curves of Na, NaO and NaOH as a function of residence time in the flow tube, in the absence of H_2 (thin lines) and in the presence of [H_2] = 1.7×10^{14} molecule cm^{-3} (thick lines). The observation point (t=2.3 ms) corresponds to the position of the resonance absorption optical

path. Panel (b): the increase in atomic absorption signal by addition of H_2 (red squares, right axis) is fitted to a set of numerical simulations (i.e. last data point of the Na curves in panel (a)) by floating the branching ratio of R3a. The modelled concentrations of NaO and NaOH are also shown. Panel (c): Back-to-back measurements of S_{40} with H_2O and H_2, showing essentially the same NaOH maximum concentration for both R2 and R3.

Figure 10. Determination of k_6. Panel (a): Decays of NaO (S_{23}) with increasing [CO] for three different contact times (P = 2 Torr, T = 300 - 320 K) fitted using the analytical expression E7 (thick lines) and simulated profiles from a numerical model (thin lines). Panel (b): k_6 results for different contact times from analytical (black) and numerical fits (red).

Figure 11. Determination of k_4. Panel (a): Decays of NaOH for increasing CO_2 at three different pressures (fixed contact time t = 5 ms). Panel (b): pressure dependence of the NaOH+ CO_2 reaction. For comparison, the only previous determination reported in the literature (dashed thick line, with uncertainty range indicated by dashed thin lines),[17] and a linear fit to the present's work data (solid thin line) are also shown. In addition a RRKM fit (MESMER, see text) is included where the only parameter floated is ΔE_{down}.

Figure 12. Simulation of the Na layer concentration with varying altitude. Red curve: Na layer 1-D model simulation for LAT and TIME[74] with the new rate constant for NaO + H_2O. Blue curve: simulation with the new rate constants for NaO + H_2O and NaOH + CO_2. Black curve: simulation with the new rate constants and the value of k(NaOH + H) required to match the field observations.

Figure 13. Removal rates of CO, O and CO_2 in the Martian atmosphere, at varying altitude during day and night-time.
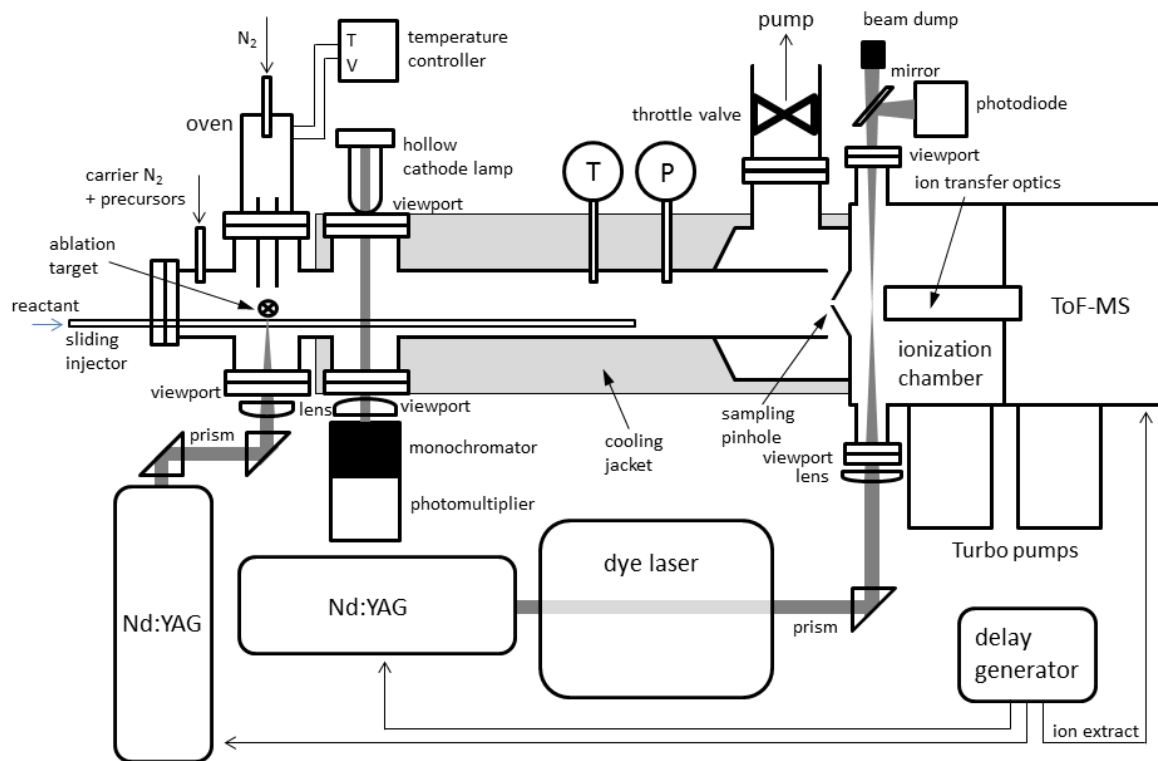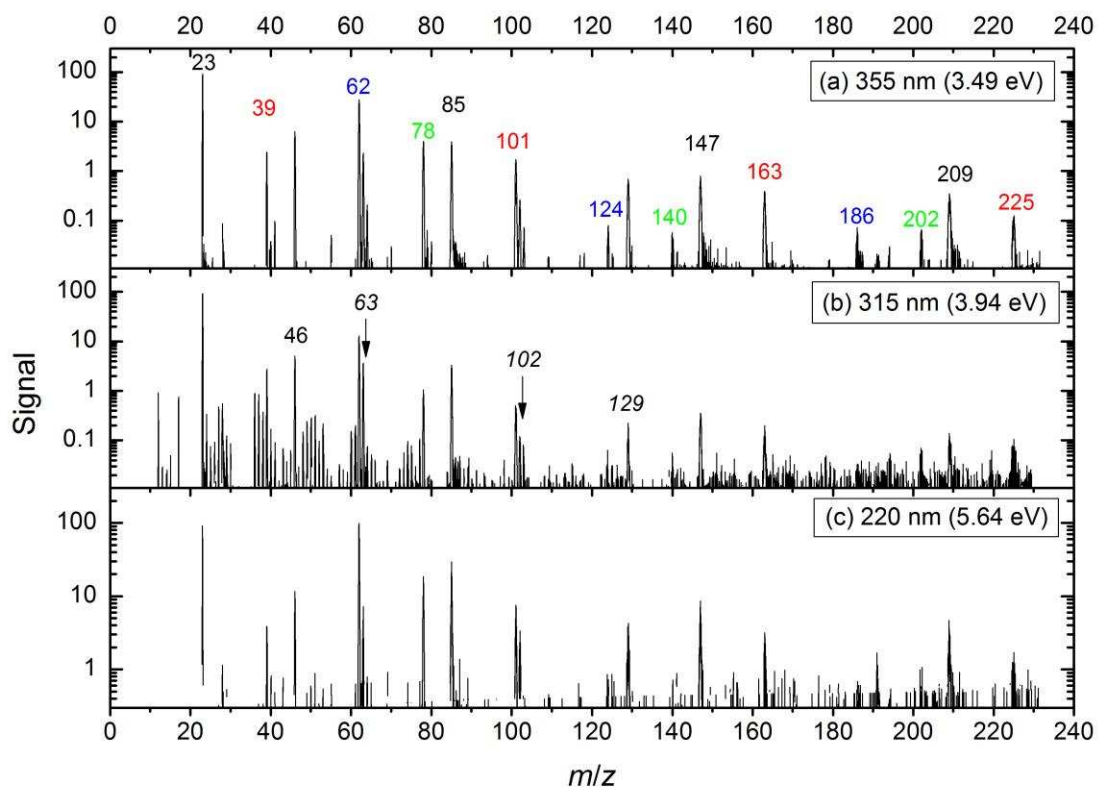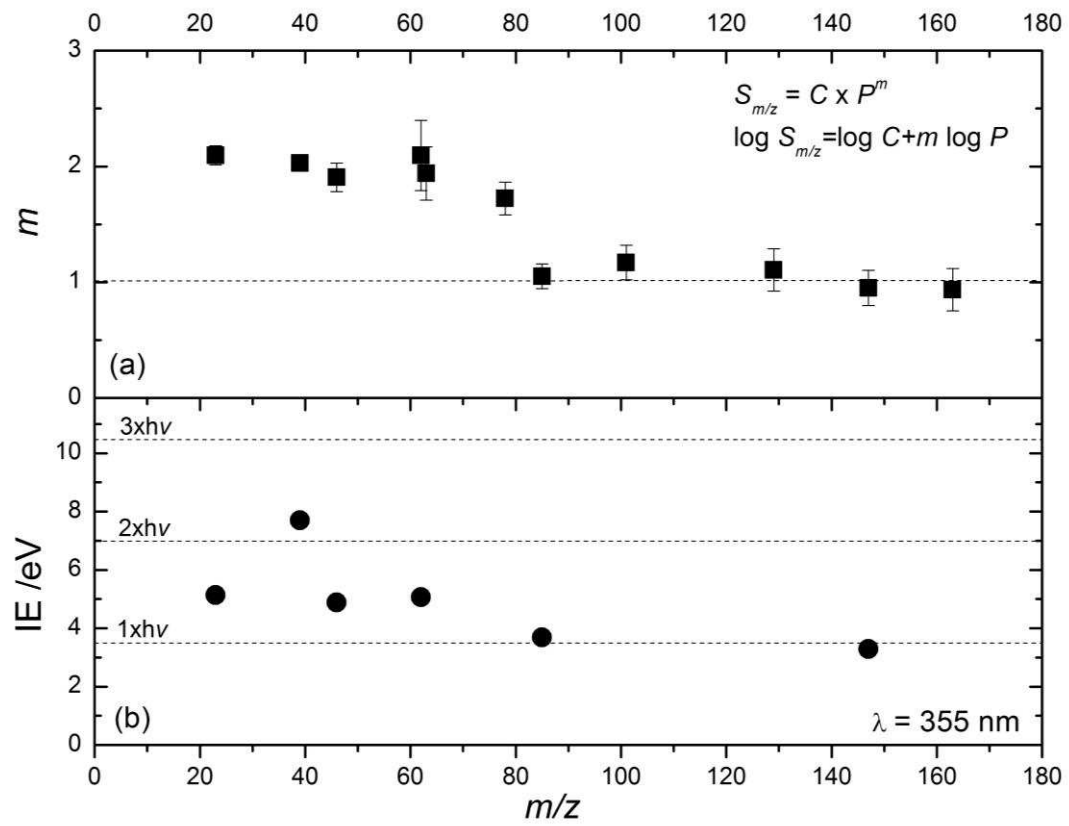
Figures

Figure 1

Figure 2

Figure 3

Figure 4
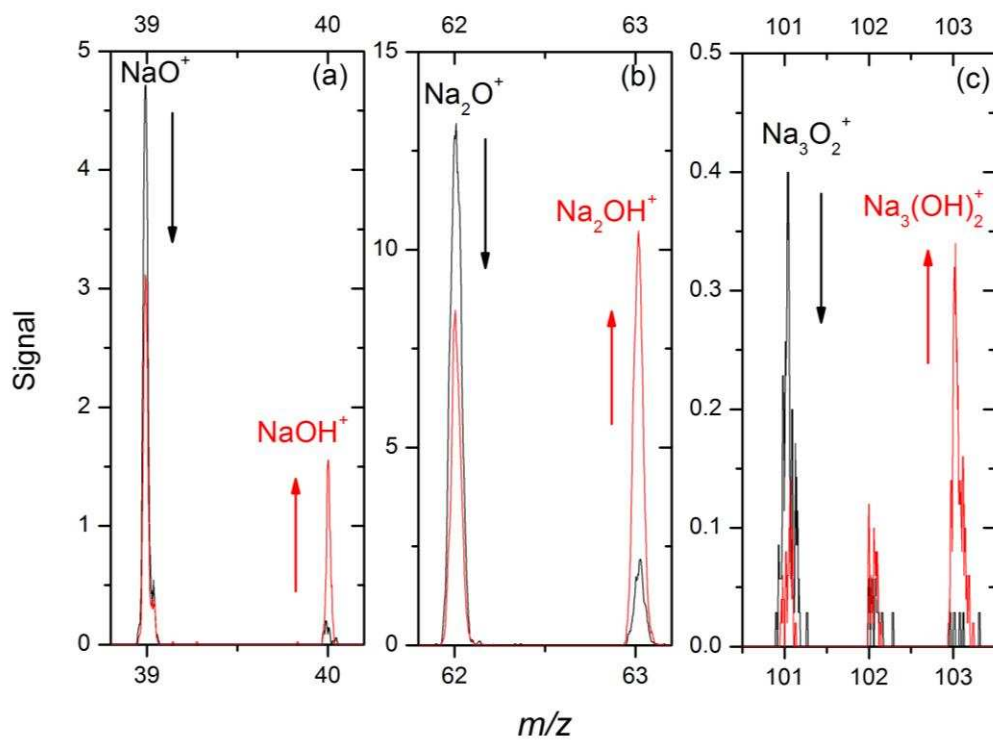
Figure 5
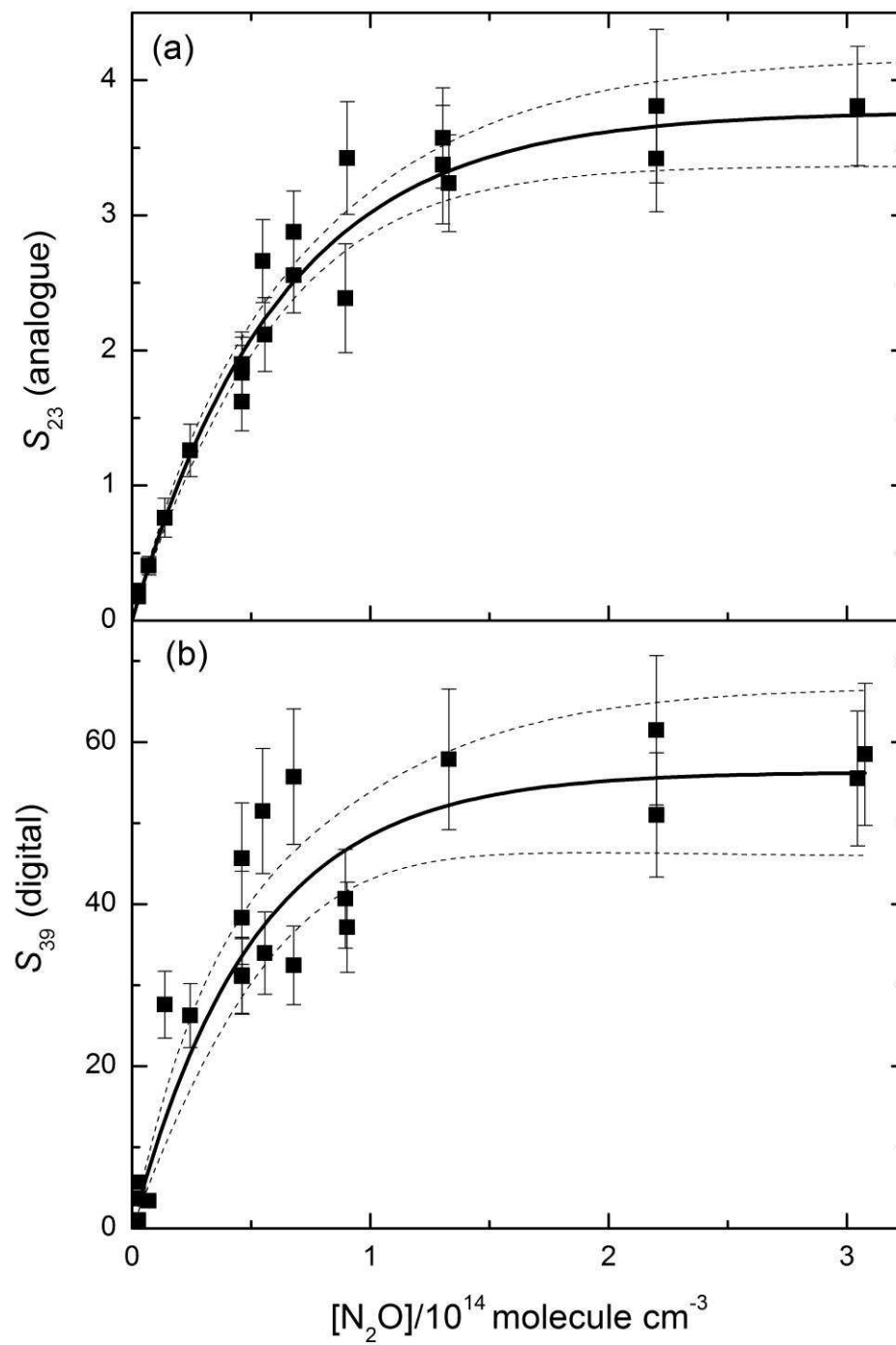
Figure 6
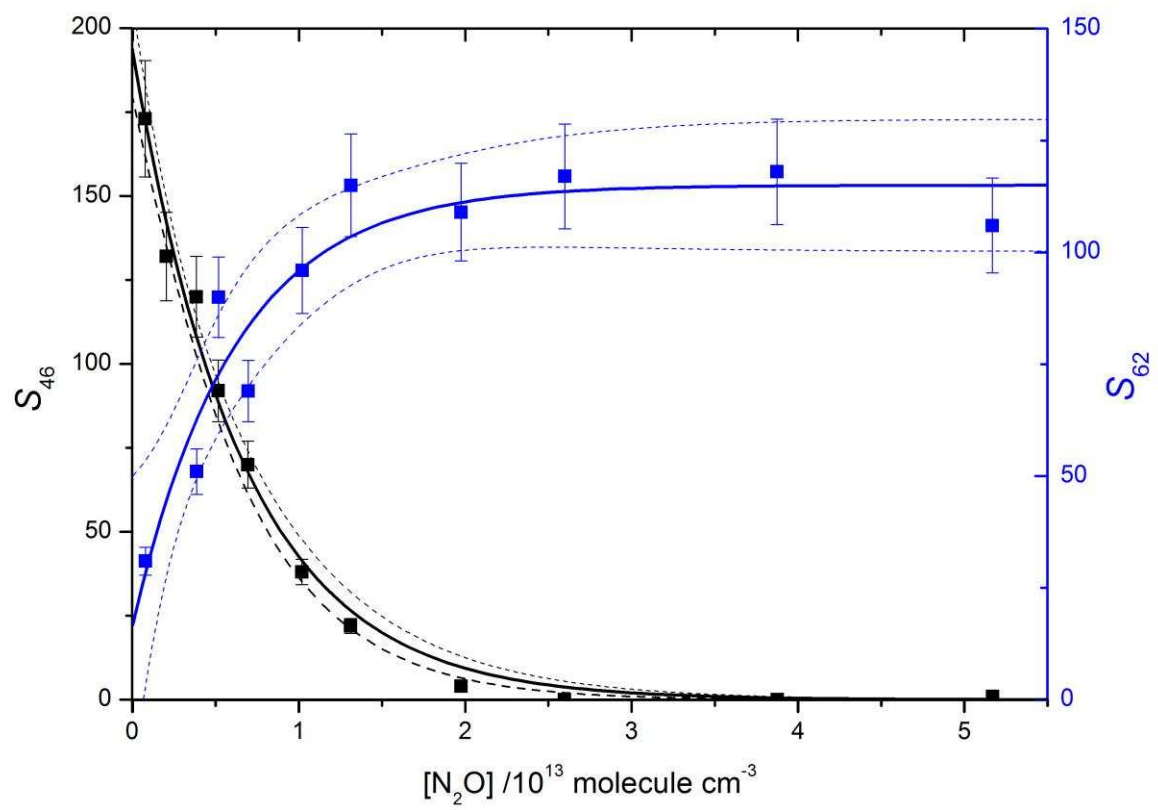
Figure 7
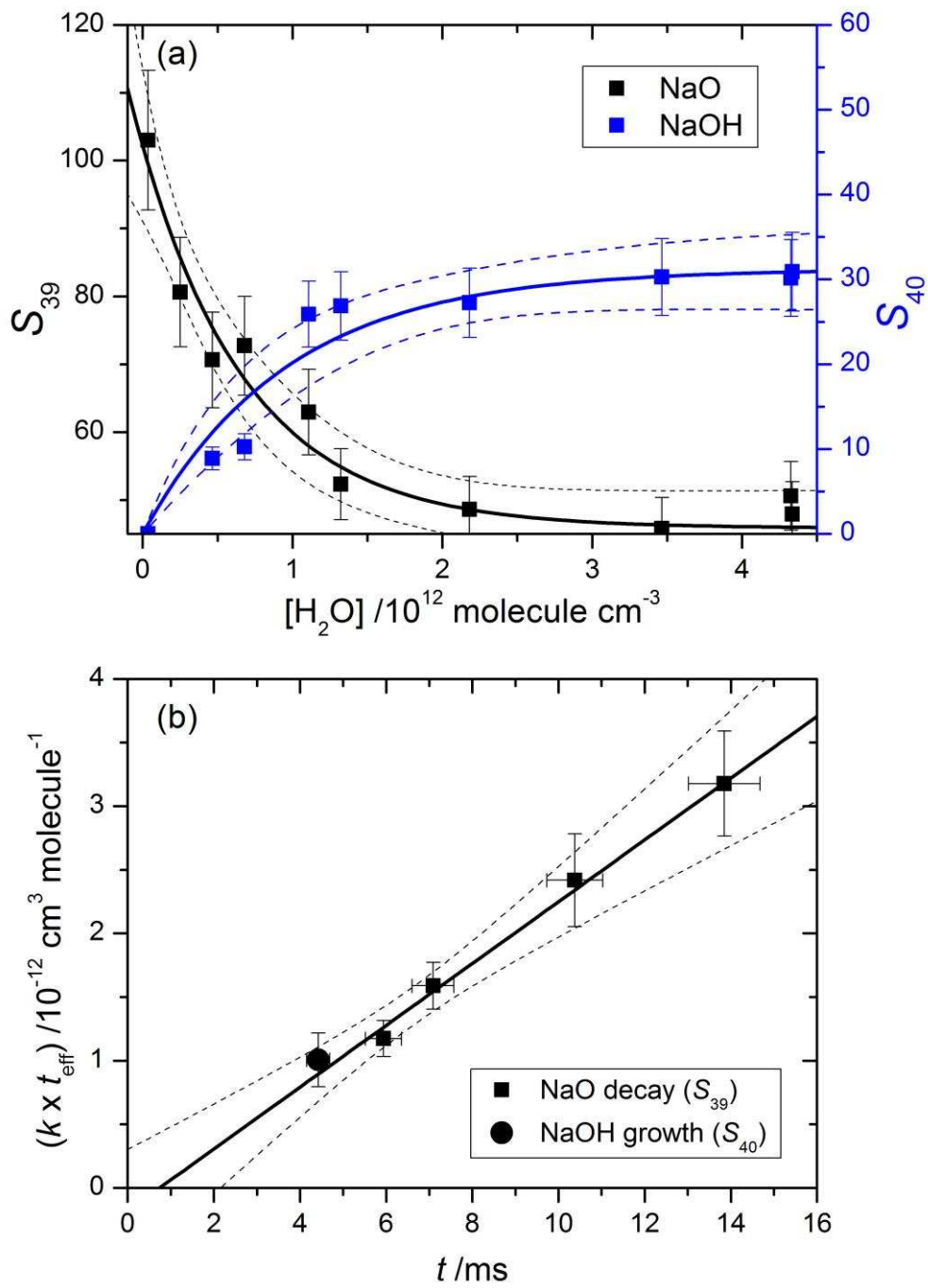
Figure 8
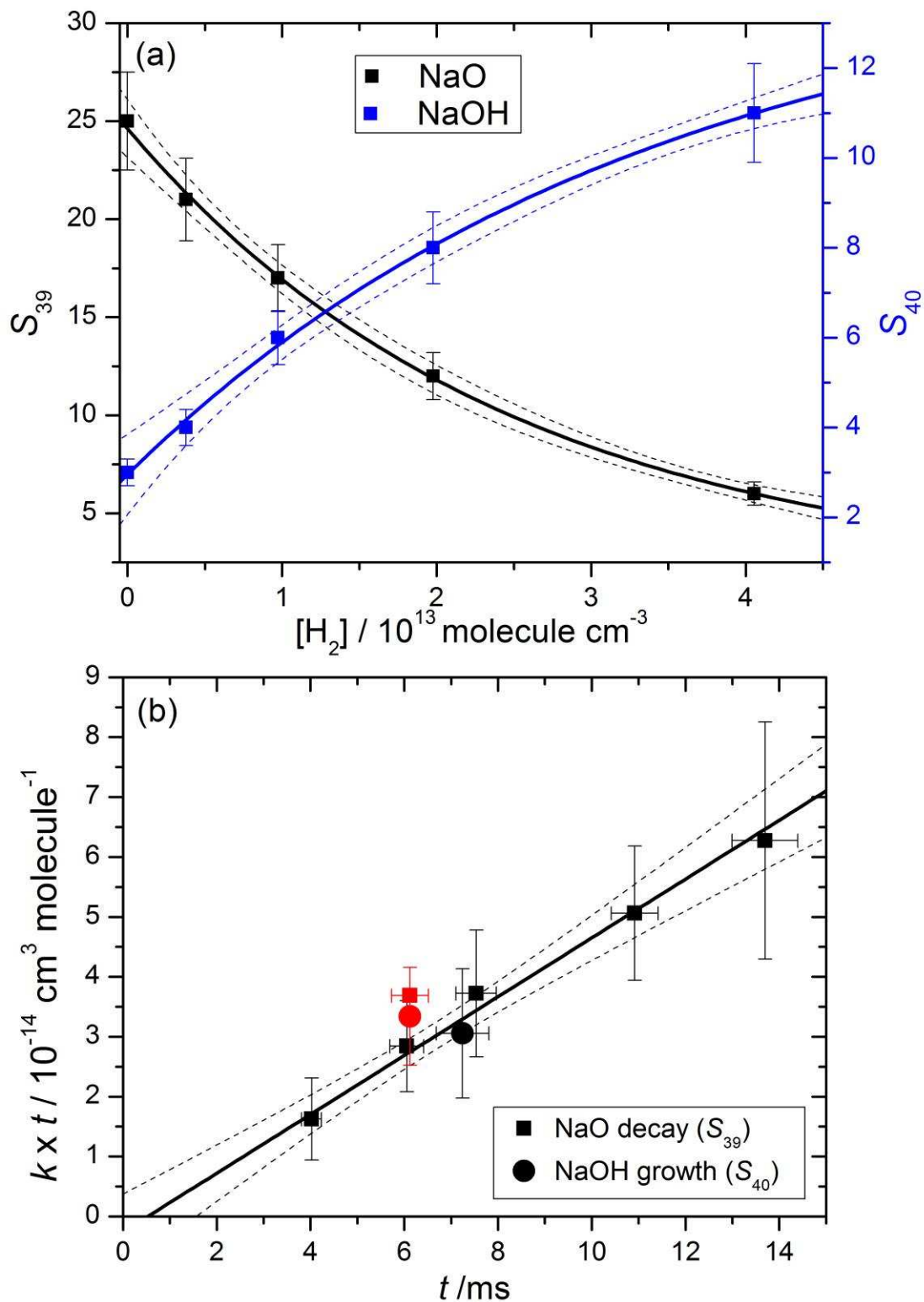
Figure 9
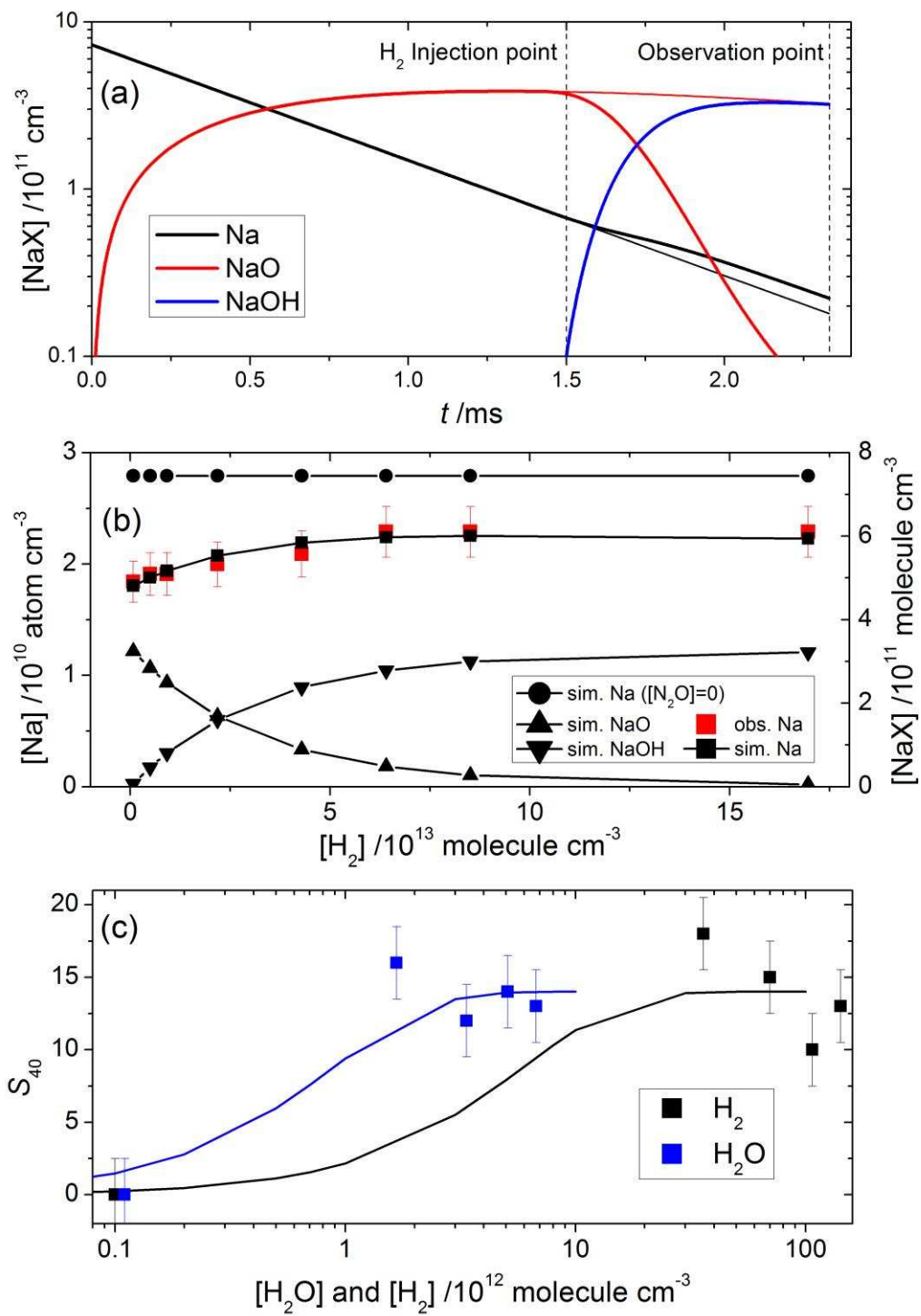
Figure 10
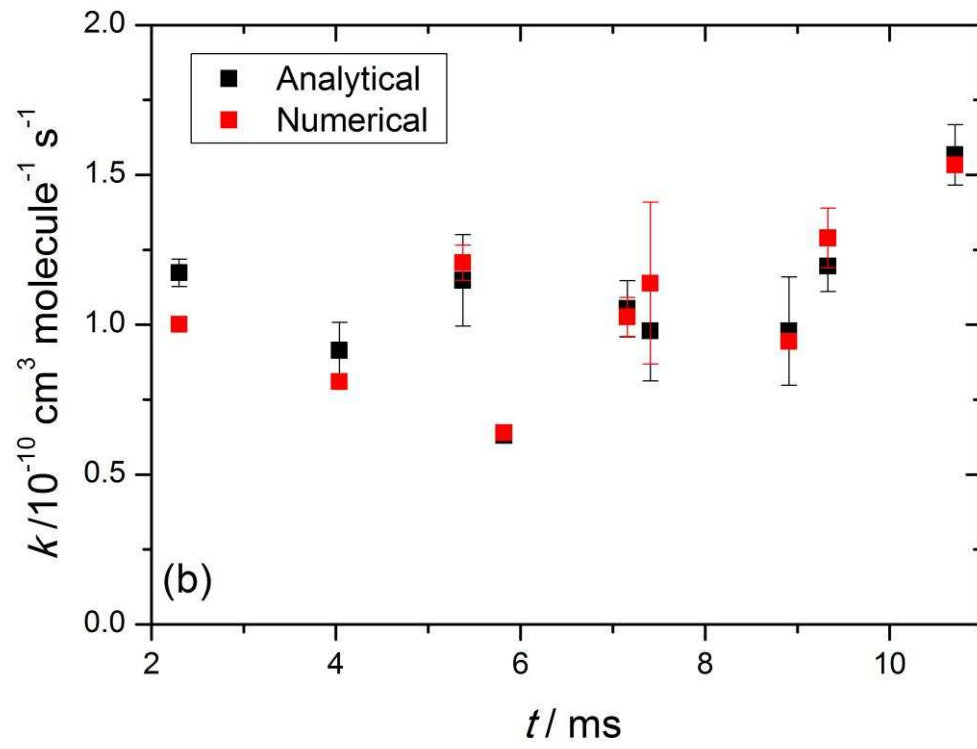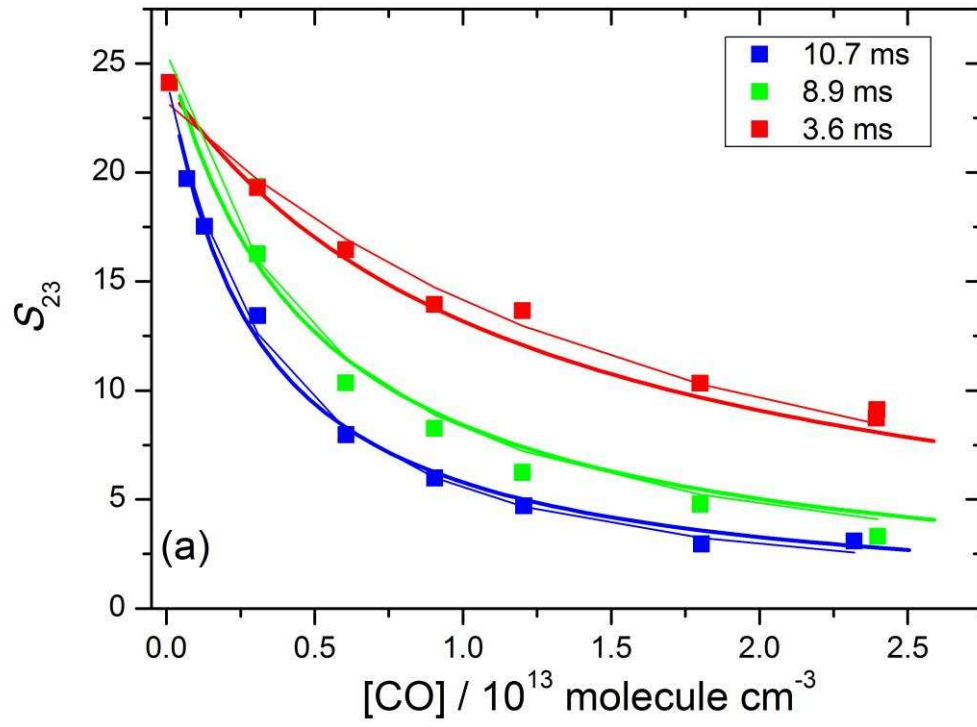
Figure 11

Figure 12

Figure 13

Mars: daytime reaction rates of NaO

References

(1) Plane, J. M. C., Cosmic Dust in the Earth's Atmosphere. Chem. Soc. Rev. **2012,** 41 (19), 6507-6518.

(2) Plane, J. M. C., Atmospheric Chemistry of Meteoric Metals. Chem. Rev. **2003,** 103, 4963 - 4984.
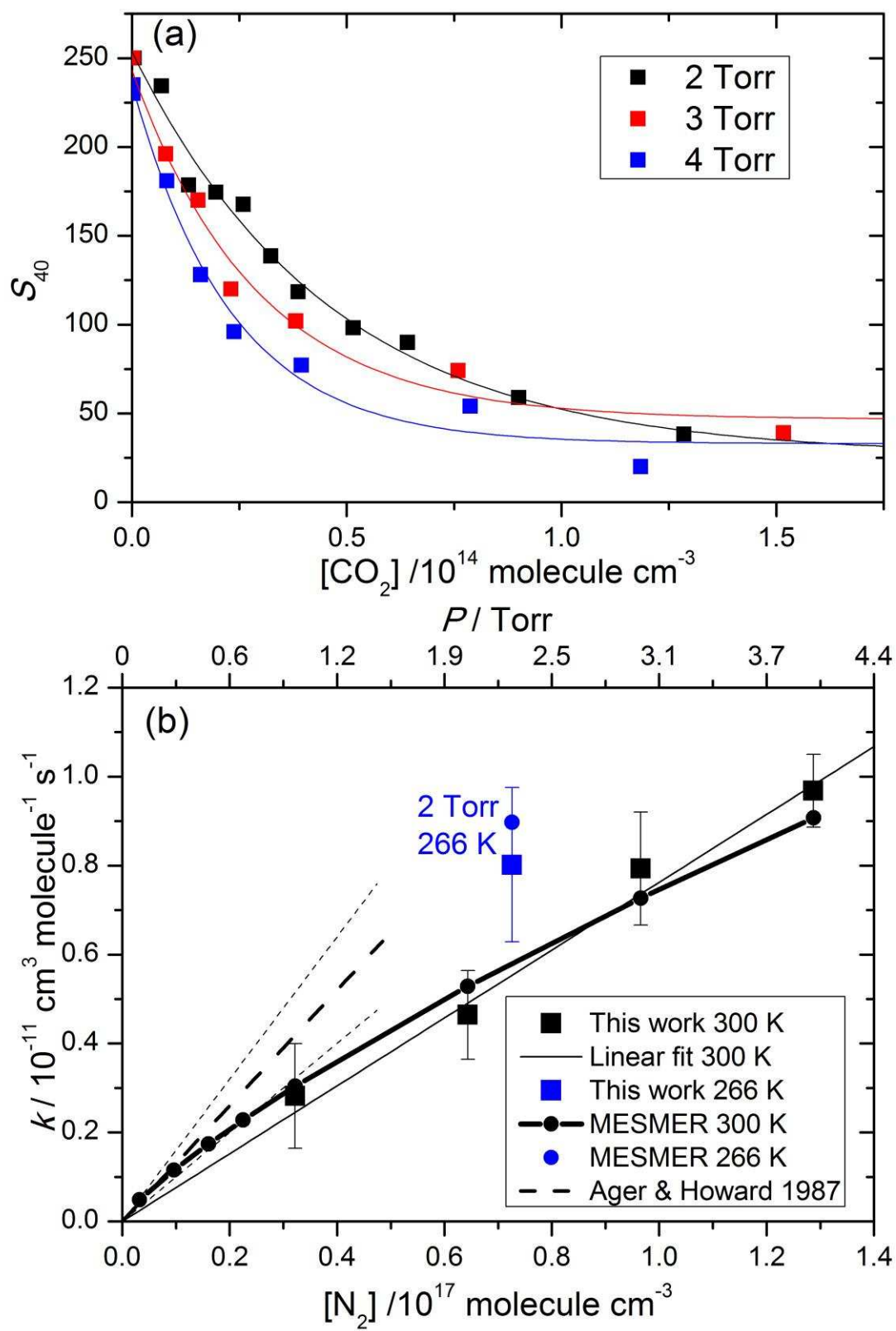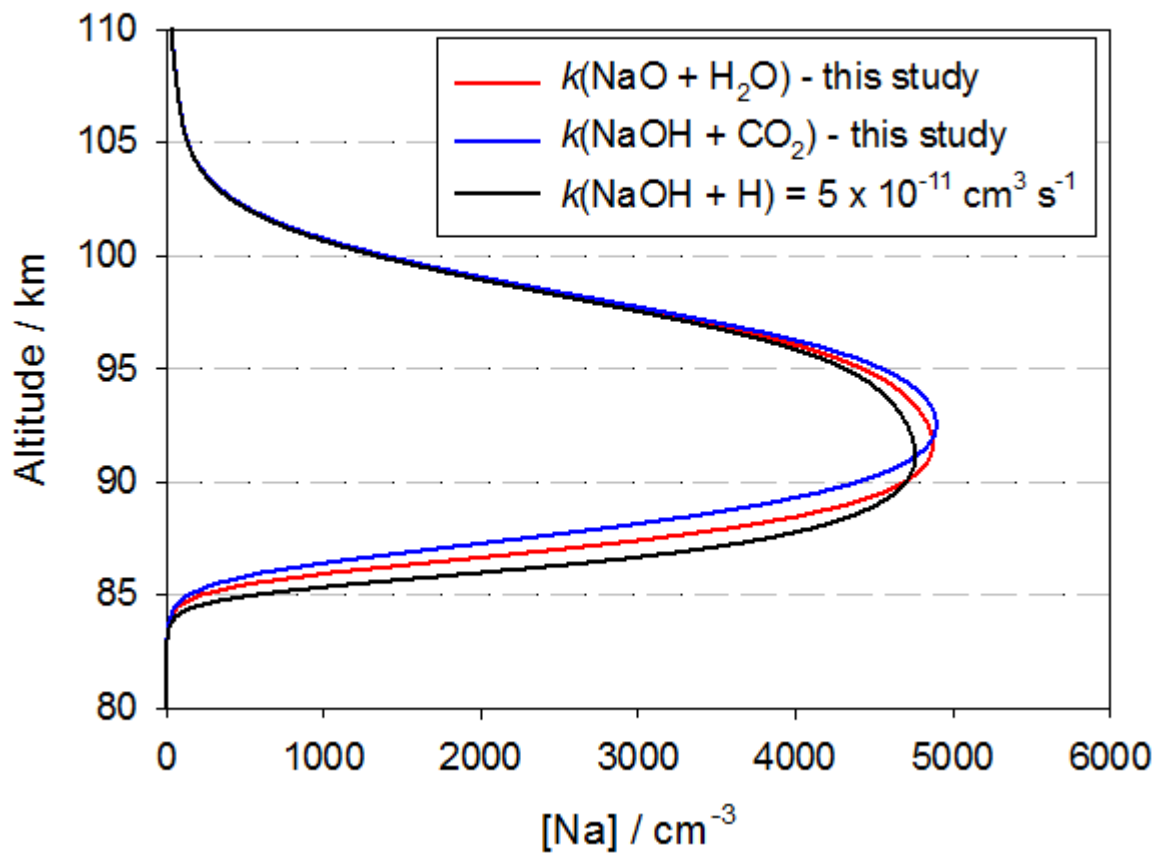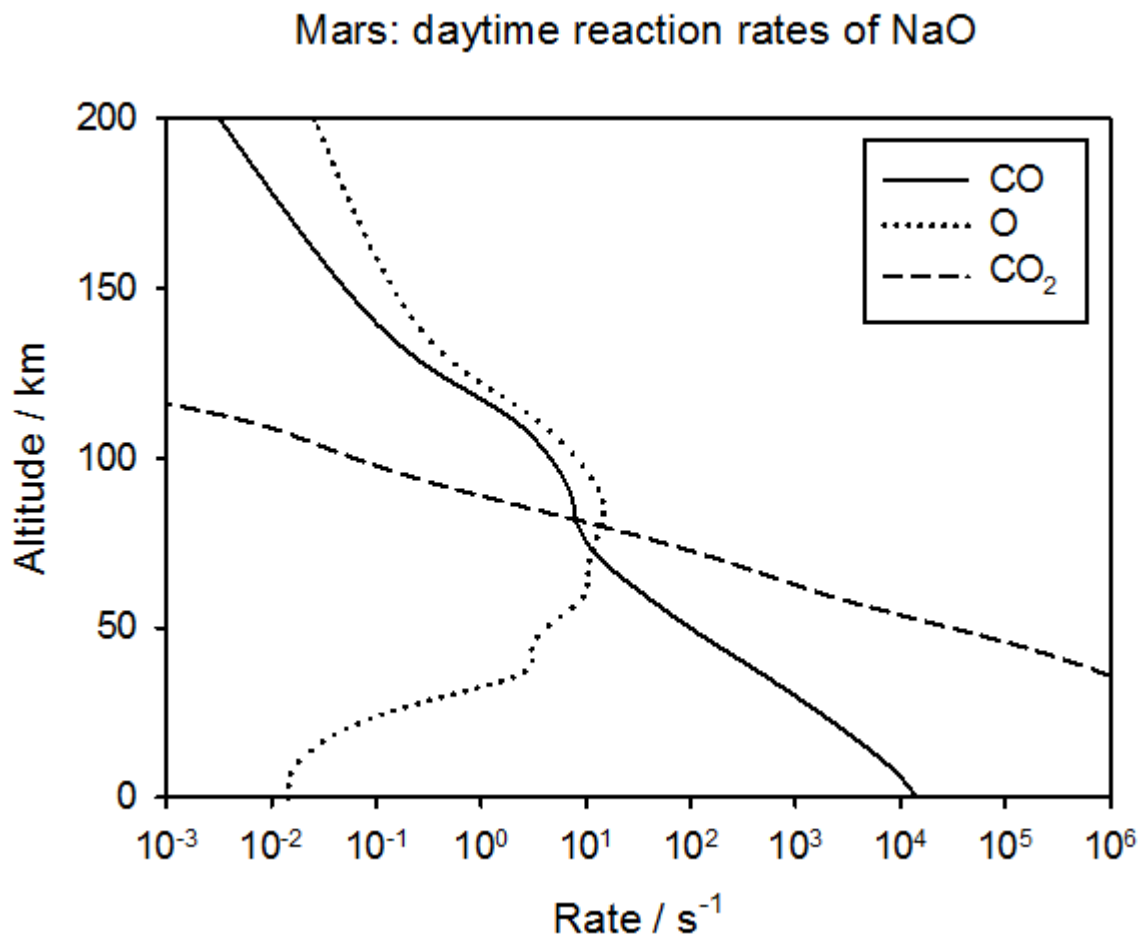
(3) Plane, J. M. C.; Cox, R. M.; Rollason, R. J., Metallic Layers in the Mesopause and Lower Thermosphere Region. Adv. Space Res. **1999,** 24 (11), 1559-1570.

(4) Chase Jr., M. W., NIST-JANAF Themochemical Tables, 4th ed. American Institute of Physics: Melville, NY, 1998.

(5) Cox, J. D.; Wagman, D. D.; Medvedev, V. A., CODATA Key Values for Thermodynamics. Hemisphere: New York, 1989.

(6) Ruscic, B.; Pinzon, R. E.; Morton, M. L.; Srinivasan, N. K.; Su, M.-C.; Sutherland, J. W.; Michael, J. V., Active Thermochemical Tables: Accurate Enthalpy of Formation of Hydroperoxyl Radical, HO2†. J. Phys. Chem. A **2006,** 110 (21), 6592-6601.

(7) Montgomery, J. A.; Frisch, M. J.; Ochterski, J. W.; Petersson, G. A., A Complete Basis Set Model Chemistry. VI. Use of Density Functional Geometries and Frequencies. J. Chem. Phys. **1999,** 110 (6), 2822-2827.

(8) Frisch, M. J.; Trucks, G. W.; Schlegel, H. B.; Scuseria, G. E.; Robb, M. A.; Cheeseman, J. R.; Scalmani, G.; Barone, V.; Mennucci, B.; Petersson, G. A.; Nakatsuji, H.; Caricato, M.; Li, X.; Hratchian, H. P.; Izmaylov, A. F.; Bloino, J.; Zheng, G.; Sonnenberg, J. L.; Hada, M.; Ehara, M.; Toyota, K.; Fukuda, R.; Hasegawa, J.; Ishida, M.; Nakajima, T.; Honda, Y.; Kitao, O.; Nakai, H.; Vreven, T.; J. A. Montgomery, J.; Peralta, J. E.; Ogliaro, F.; Bearpark, M.; Heyd, J. J.; Brothers, E.; Kudin, K. N.; Staroverov, V. N.; Kobayashi, R.; Normand, J.; Raghavachari, K.; Burant, A. R. J. C.; Iyengar, S. S.; Tomasi, J.; Cossi, M.; Rega, N.; Millam, J. M.; Klene, M.; Knox, J. E.; Cross, J. B.; Bakken, V.; Adamo, C.; Jaramillo, J.;

Gomperts, R.; Stratmann, R. E.; Yazyev, O.; Austin, A. J.; Cammi, R.; Pomelli, C.; Ochterski, J. W.; Martin, R. L.; Morokuma, K.; Zakrzewski, V. G.; Voth, G. A.; Salvador, P.; Dannenberg, J. J.; Dapprich, S.; Daniels, A. D.; Farkas, Ö.; Foresman, J. B.; Ortiz, J. V.; Cioslowski, J.; Fox, D. J. Gaussian 09, Revision D.01, Gaussian, Inc.: Wallingford CT, 2009.

(9) Jensen, D. E.; Jones, G. A., Kinetics of Flame Inhibition by Sodium. J. Chem. Soc., Faraday Trans. 1 **1982,** 78 (9), 2843-2850.

(10) Silver, J. A.; Stanton, A. C.; Zahniser, M. S.; Kolb, C. E., Gas-Phase Reaction Rate of Sodium Hydroxide with Hydrochloric Acid. J. Phys. Chem. **1984,** 88 (14), 3123-3129.

(11) Ager III, J. W.; Howard, C. J., Gas Phase Kinetics of the Reactions of NaO with H_2, D_2, H_2O, and D_2O. J. Chem. Phys. **1987,** 87 (2), 921-925.

(12) Cox, R. M.; Plane, J. M., An Experimental and Theoretical Study of the Reactions NaO+ H_2O (D_2O)→ NaOH (D)+ OH (OD). Phys. Chem. Chem. Phys. **1999,** 1 (20), 4713-4720.

(13) Self, D. E.; Plane, J. M., Absolute Photolysis Cross-Sections for $NaHCO_3$, NaOH, NaO, NaO_2 and NaO_3: Implications for Sodium Chemistry in the Upper Mesosphere. Phys. Chem. Chem. Phys. **2002,** 4 (1), 16-23.

(14) Cox, R. M.; Self, D. E.; Plane, J., A Study of the Reaction Between NaHCO3 and H: Apparent Closure on the Chemistry of Mesospheric Na. J. Geophys. Res. [Atmos.] **2001,** 106 (D2), 1733-1739.

(15) Plane, J. M. C.; Husain, D., Determination of the Absolute Rate Constant for the Reaction O + NaO → Na + O_2 by Time-Resolved Atomic Chemiluminescence at $\lambda = 589$ nm [Na(3 ^{2}P) →Na(3 $^2S_{1/2}$) + hv]. J. Chem. Soc., Faraday Trans. 2 **1986,** 82 (11), 2047-2052.

(16) Stoecklin, T.; Clary, D. C., Fast Reactions between Diatomic and Polyatomic Molecules. J. Phys. Chem. **1992,** 96 (18), 7346-7351.

(17) Ager, J. W.; Howard, C. J., Rate Coefficient for the Gas Phase Reaction of NaOH with CO_2. J. Geophys. Res. [Atmos.] **1987,** 92 (D6), 6675-6678.

(18) Ager, J. W.; Howard, C. J., The kinetics of NaO + O2 + M and NaO + CO2 + M and their role in atmospheric sodium chemistry. Geophysical Research Letters **1986,** 13 (13), 1395-1398.

(19) Pugh, J. V.; Shen, K. K.; Winstead, C. B.; Gole, J. L., Accessing a Low-Lying Bound Electronic State of the Alkali Oxides, LiO and NaO, Using Laser Induced Fluorescence. Chem. Phys. **1996,** 202 (1), 129-138.

(20) Hildenbrand, D. L.; Murad, E., Dissociation Energy of NaO(g) and the Heat of Atomization of Na_2O(g). J. Chem. Phys. **1970,** 53 (9), 3403-3408.

(21) Schoonmaker, R. C.; Porter, R. F., Gaseous Species in the Vaporization of Sodium Hydroxide. J. Chem. Phys. **1958,** 28 (3), 454-457.

(22) Peterson, K. I.; Dao, P. D.; Castleman, A. W., Photoionization Studies of Na_2Cl and Na_2O and Reactions of Metal Clusters. J. Chem. Phys. **1983,** 79 (2), 777-783.

(23) Dao, P. D.; Peterson, K. I.; Castleman, A. W., The Photoionization of Oxidized Metal Clusters. J. Chem. Phys. **1984,** 80 (1), 563-564.

(24) Hampe, O.; Koretsky, G. M.; Gegenheimer, M.; Huber, C.; Kappes, M. M.; Gauss, J., On the Ground and Electronically Excited States of Na_3O: Theory and Experiment. J. Chem. Phys. **1997,** 107 (18), 7085-7095.

(25) Vituccio, D. T.; Herrmann, R. F. W.; Golonzka, O.; Ernst, W. E., New Measurements of Appearance Potentials and Optical Absorption of Na_2F and Na_3O. J. Chem. Phys. **1997,** 106 (10), 3865-3869.

(26) Elliott, S. D.; Ahlrichs, R., An Ab Initio Study of the Monoxides and Dioxides of Sodium. J. Chem. Phys. **1998,** 109 (11), 4267-4280.

(27) Buck, U.; Steinbach, C., Formation of Sodium Hydroxyde in Multiple Sodium−Water Cluster Collisions. J. Phys. Chem. A **1998,** 102 (38), 7333-7336.

(28) Goerke, A.; Leipelt, G.; Palm, H.; Schulz, C. P.; Hertel, I. V., Reactive Scattering of Sodium Clusters with Molecular Oxygen. Z. Phys. D: At., Mol. Clusters **1995,** 32 (4), 311-320.

(29) Husain, D.; Plane, J. M. C., Kinetic Investigation of the Reaction between $Na + O_2 + M$ by Time-Resolved Atomic Resonance Absorption Spectroscopy. J. Chem. Soc., Faraday Trans. 2 **1982,** 78 (1), 163-178.

(30) Fricke, K. H.; von Zahn, U., Mesopause Temperatures Derived from Probing the Hyperfine Structure of the D2 Resonance Line of Sodium by Lidar. J. Atmos. Terr. Phys. **1985,** 47 (5), 499-512.

(31) Self, D. E.; Plane, J. M. C., A Kinetic Study of the Reactions of Iron Oxides and Hydroxides Relevant to the Chemistry of Iron in the Upper Mesosphere. Phys. Chem. Chem. Phys. **2003,** 5 (7), 1407-1418.

(32) Talcott, C. L.; Ager, J. W.; Howard, C. J., Gas Phase Studies of Na Diffusion in He and Ar and Kinetics of $Na + Cl_2$ and $Na + SF_6$. J. Chem. Phys. **1986,** 84 (11), 6161-6169.

(33) Howard, C. J., Kinetic Measurements Using Flow Tubes. J. Phys. Chem. **1979,** 83 (1), 3-9.

(34) Kung, A.; Young, J. F.; Harris, S., Generation of 1182 Å Radiation in Phase-Matched Mixtures of Inert Gases. Appl. Phys. Lett. **2003,** 22 (6), 301-302.

(35) Blitz, M. A.; Goddard, A.; Ingham, T.; Pilling, M. J., Time-of-Flight Mass Spectrometry for Time-Resolved Measurements. Rev. Sci. Instrum. **2007,** 78 (3), 034103.

(36) Hooker, S. M.; Webb, C. E., Progress in Vacuum Ultraviolet Lasers. Prog. Quant. Electron. **1994,** 18 (3), 227-274.

(37) Hanna, S. J.; Campuzano-Jost, P.; Simpson, E. A.; Robb, D. B.; Burak, I.; Blades, M. W.; Hepburn, J. W.; Bertram, A. K., A New Broadly Tunable (7.4–10.2 eV) Laser Based VUV Light Source and its First Application to Aerosol Mass Spectrometry. Int. J. Mass spectrom. **2009,** 279 (2–3), 134-146.

(38) Robertson, S. H.; Glowacki, D. R.; Liang, C.-H.; Morley, C.; Shannon, R.; Blitz, M.; Pilling, M. J. MESMER (Master Equation Solver for Multi-Energy Well Reactions). http://sourceforge.net/projects/mesmer.

(39) Glowacki, D. R.; Liang, C.-H.; Morley, C.; Pilling, M. J.; Robertson, S. H., MESMER: An Open-Source Master Equation Solver for Multi-Energy Well Reactions. J. Phys. Chem. A **2012,** 116 (38), 9545-9560.

(40) Frisch, M. J.; Trucks, G. W.; Schlegel, H. B.; Scuseria, G. E.; Robb, M. A.; Cheeseman, J. R.; Scalmani, G.; Barone, V.; Mennucci, B.; Petersson, G. A.; Nakatsuji, H.; Caricato, M.; Li, X.; Hratchian, H. P.; Izmaylov, A. F.; Bloino, J.; Zheng, G.; Sonnenberg, J. L.; Hada, M.; Ehara, M.; Toyota, K.; Fukuda, R.; Hasegawa, J.; Ishida, M.; Nakajima, T.; Honda, Y.; Kitao, O.; Nakai, H.; Vreven, T.; Montgomery Jr., J. A.; Peralta, J. E.; Ogliaro, F.; Bearpark, M. J.; Heyd, J.; Brothers, E. N.; Kudin, K. N.; Staroverov, V. N.; Kobayashi, R.; Normand, J.; Raghavachari, K.; Rendell, A. P.; Burant, J. C.; Iyengar, S. S.; Tomasi, J.; Cossi, M.; Rega, N.; Millam, N. J.; Klene, M.; Knox, J. E.; Cross, J. B.; Bakken, V.; Adamo, C.; Jaramillo, J.; Gomperts, R.; Stratmann, R. E.; Yazyev, O.; Austin, A. J.; Cammi, R.; Pomelli, C.; Ochterski, J. W.; Martin, R. L.; Morokuma, K.; Zakrzewski, V. G.; Voth, G. A.; Salvador, P.; Dannenberg, J. J.; Dapprich, S.; Daniels, A. D.; Farkas, Ö.; Foresman, J. B.; Ortiz, J. V.; Cioslowski, J.; Fox, D. J. Gaussian 09, Gaussian, Inc.: Wallingford, CT, USA, 2009.

(41) Robertson, S. H.; Pilling, M. J.; Baulch, D. L.; Green, N. J. B., Fitting of pressure-dependent kinetic rate data by master equation/inverse Laplace transform analysis. J. Phys. Chem. **1995,** 99 (36), 13452-13460.

(42) Davies, J. W.; Green, N. J. B.; Pilling, M. J., The Testing of Models for Unimolecular Decomposition Via Inverse Laplace Transformation of Experimental Recombination Rate Data. Chem. Phys. Lett. **1986,** 126 (3–4), 373-379.

(43) London, F., The General Theory of Molecular Forces. Trans. Faraday Soc. **1932,** 33 (8).

(44) Georgievskii, Y.; Klippenstein, S. J., Long-Range Transition State Theory. J. Chem. Phys. **2005,** 122 (19), 194103.

(45) Stoecklin, T.; Dateo, C. E.; Clary, D. C., Rate Constant Calculations on Fast Diatom-Diatom Reactions. J. Chem. Soc., Faraday Trans. **1991,** 87 (11), 1667-1679.

(46) Elliott, S. D.; Ahlrichs, R.; Hampe, O.; Kappes, M. M., Auto-Ionised Products from the Reaction of Sodium Clusters with Dioxygen: Theory and Experiment. Phys. Chem. Chem. Phys. **2000,** 2 (15), 3415-3424.

(47) Gomez Martin, J. C.; Plane, J. M. C., Formation of Sodium Oxide Clusters at Thermal Energies: Experiments and Theory. **2015,** In preparation.

(48) Lide, D. R., Handbook of Chemistry and Physics. 73 ed.; CRC: Boca Raton, Florida, 1992.

(49) Hudson, R. D., Measurements of the Molecular Absorption Cross Section and the Photoionization of Sodium Vapor between 1600 and 3700 Å. J. Chem. Phys. **1965,** 43 (5), 1790-1793.

(50) Soldán, P.; Lee, E. P. F.; Wright, T. G., Spectroscopy and Thermodynamics of $NaO^+(X^3\Sigma^-)$: Relevance to Atmospheric Chemistry. J. Phys. Chem. A **1998,** 102 (45), 9040-9046.

(51) Soldán, P.; Lee, E. P.; Gamblin, S. D.; Wright, T. G., Photoionization of NaO ($X^2\Pi$; $A^2\Sigma^+$) and the Absorption/Emission Spectra of the Lowest Cationic States. Phys. Chem. Chem. Phys. **1999,** 1 (21), 4947-4954.

(52) Ledingham, K. W. D.; Singhal, R. P., High Intensity Laser Mass Spectrometry — a Review. Int. J. Mass Spectrom. Ion Processes **1997,** 163 (3), 149-168.

(53) Andrews, L., Ultraviolet Absorption Studies of the Alkali Metal Atom-Oxygen Molecule Matrix Reaction. J. Mol. Spectrosc. **1976,** 61 (3), 337-345.

(54) Plane, J. M. C., A Comparison between the Oxidation Reactions of the Alkali and Alkaline Earth Atoms. In Gas Phase Metal Reactions, Fontijn, A., Ed. Elsevier: Amsterdam, 1992; pp 29-56.

(55) Plane, J. M. C.; Rajasekhar, B., Kinetic Study of the Reactions Sodium + Oxygen + Nitrogen and Sodium + Nitrous Oxide over an Extended Temperature Range. J. Phys. Chem. **1989,** 93 (8), 3135-3140.

(56) Ager, J. W.; Talcott, C. L.; Howard, C. J., Gas Phase Kinetics of the Reactions of Na and NaO with O_3 and N_2O. J. Chem. Phys. **1986,** 85 (10), 5584-5592.

(57) Worsnop, D. R.; Zahniser, M. S.; Kolb, C. E., Low-Temperature Absolute Rate Constants for the Reaction of Atomic Sodium with Ozone and Nitrous Oxide. J. Phys. Chem. **1991,** 95 (10), 3960-3964.

(58) Silver, J. A., Measurement of Atomic Sodium and Potassium Diffusion Coefficients. J. Chem. Phys. **1984,** 81 (11), 5125-5130.

(59) Sander, S. P.; Abbatt, J.; Barker, J. R.; Burkholder, J. B.; Friedl, R. R.; Golden, D. M.; Huie, R. E.; Kolb, C. E.; Kurylo, M. J.; Moortgat, G. K.; Orkin, V. L.; Wine, P. H. Chemical Kinetics and Photochemical Data for Use in Atmospheric Studies, Evaluation No. 17," JPL Publication 10-6; Jet Propulsion Laboratory: Pasadena, 2011; http://jpldataeval.jpl.nasa.gov.

(60) Helmer, M.; Plane, J. M. C., A Study of the Reaction $NaO_2 + O \rightarrow NaO + O_2$: Implications for the Chemistry of Sodium in the Upper Atmosphere. J. Geophys. Res. [Atmos.] **1993,** 98 (D12), 23207-23222.

(61) Joo, S.; Worsnop, D. R.; Kolb, C. E.; Kim, S. K.; Herschbach, D. R., Observation of the $A^2\Sigma^+ \leftarrow X^2\Pi$ Electronic Transition of NaO. J. Phys. Chem. A **1999,** 103 (17), 3193-3199.

(62) Wright, T. G.; Ellis, A. M.; Dyke, J. M., A Study of the Products of the Gas-Phase Reactions M + N₂O and M + O₃, where M = Na or K, with Ultraviolet Photoelectron Spectroscopy. J. Chem. Phys. **1993,** 98 (4), 2891-2907.

(63) Shi, X.; Herschbach, D. R.; Worsnop, D. R.; Kolb, C. E., Molecular Beam Chemistry: Magnetic Deflection Analysis of Monoxide Electronic States from Alkali-Metal Atom + Ozone Reactions. J. Phys. Chem. **1993,** 97 (10), 2113-2122.

(64) Plane, J.; Oetjen, H.; de Miranda, M.; Saiz-Lopez, A.; Gausa, M.; Williams, B., On the Sodium D Line Emission in the Terrestrial Nightglow. J. Atmos. Sol. Terr. Phys. **2012,** 74 (0), 181-188.

(65) Plane, J. M. C.; Nien, C. F.; Allen, M. R.; Helmer, M., A Kinetic Investigation of the Reactions Sodium + Ozone and Sodium Monoxide + Ozone over the Temperature Range 207-377 K. J. Phys. Chem. **1993,** 97 (17), 4459-4467.

(66) Griffin, J.; Worsnop, D. R.; Brown, R. C.; Kolb, C. E.; Herschbach, D. R., Chemical Kinetics of the NaO ($A^2\Sigma^+$) + O(^{3}P) Reaction. J. Phys. Chem. A **2000,** 105 (9), 1643-1648.

(67) Silver, J. A.; Kolb, C. E., Determination of the Absolute Rate Constants for the Room Temperature Reactions of Atomic Sodium with Ozone and Nitrous Oxide. J. Phys. Chem. **1986,** 90 (14), 3263-3266.

(68) Vasiliu, M.; Li, S.; Peterson, K. A.; Feller, D.; Gole, J. L.; Dixon, D. A., Structures and Heats of Formation of Simple Alkali Metal Compounds: Hydrides, Chlorides, Fluorides, Hydroxides, and Oxides for Li, Na, and K. J. Phys. Chem. A **2010,** 114 (12), 4272-4281.

(69) Mintz, B.; Chan, B.; Sullivan, M. B.; Buesgen, T.; Scott, A. P.; Kass, S. R.; Radom, L.; Wilson, A. K., Structures and Thermochemistry of the Alkali Metal Monoxide Anions, Monoxide Radicals, and Hydroxides. J. Phys. Chem. A **2009,** 113 (34), 9501-9510.

(70) Ager III, J. W.; Howard, C. J., The Kinetics of NaO + O_2 + M and NaO + CO_2 + M and their Role in Atmospheric Sodium Chemistry. Geophys. Res. Lett. **1986,** 13 (13), 1395-1398.

(71) Gilbert, R. G.; Smith, S. C., Theory of Unimolecular and Recombination Reactions. Blackwell: Oxford, 1990.

(72) Hildenbrand, D. L.; Lau, K. H., Mass Spectrometric Searches for Gaseous Sodium Carbonates. J. Phys. Chem. **1991,** 95 (22), 8972-8975.

(73) Slanger, T. G.; Cosby, P. C.; Huestis, D. L.; Saiz-Lopez, A.; Murray, B. J.; O'Sullivan, D. A.; Plane, J. M. C.; Allende Prieto, C.; Martin-Torres, F. J.; Jenniskens, P., Variability of the Mesospheric Nightglow Sodium D2/D1 Ratio. J. Geophys. Res. [Atmos.] **2005,** 110 (D23), D23302.

(74) Plane, J. M. C., A Time-Resolved Model of the Mesospheric Na Layer: Constraints on the Meteor Input Function. Atmos. Chem. Phys. **2004,** 4 (3), 627-638.

(75) Molina-Cuberos, J.; López-Moreno, J.; Arnold, F., Meteoric Layers in Planetary Atmospheres. In Planetary Atmospheric Electricity, Springer: 2008; pp 175-191.

(76) Millour, E.; Forget, F.; Lewis, S. R. Mars Climate Database version 5.1, http://www-mars.lmd.jussieu.fr/, Oxford, 2014.